

Active bi- and multistability in cooperative microactuator systems

Manfred Kohl^{a,*}, Christoph Ament^b, Gowtham Arivanandhan^a, Tamara Bechtold^c, Peter Conrad^d, Sipontina Croce^g, Vincent Gottwald^a, Martin Hoffmann^d, Jonas Hubertus^h, Alexander Kopp^b, Zixiong Li^a, Michael Olbrich^b, Kirill Poletkin^{a,f}, Alberto Priuli^g, Gianluca Rizzello^g, Arwed Schuetz^c, Guenter Schultes^h, Stefan Seelecke^g, Lena Seigner^a, Hamid Shahsavari^{a,i}, Muhammad B. Shamim^j, Marian Sielenkämper^j, Georgino K. Tshikwand^e, Ulrike Wallrabe^k, Pascal Weber^k, Frank Wendler^e, Stephan Wulfinhoff^j

^a Institute of Microstructure Technology, Karlsruhe Institute of Technology, Karlsruhe 76021, Germany

^b Department of Control Engineering, University of Augsburg, Augsburg 86159, Germany

^c Jade University of Applied Sciences, Wilhelmshaven 26389, Germany

^d Department of Micromechanical Systems, Ruhr-University Bochum, Bochum 44801, Germany

^e Materials Science Department, Friedrich-Alexander University Nürnberg-Erlangen, Fürth 90762, Germany

^f School of Instrument Science and Optoelectronics Engineering, Hefei University of Technology, China

^g Department of Systems Engineering, Saarland University, Saarbrücken, Germany

^h Department of Sensors and Thin Films, University of Applied Sciences, Saarbrücken, Germany

ⁱ Department of Surgery, University of Oklahoma Health Sciences Center, Oklahoma, OK, USA

^j Institute for Materials Science, Kiel University, Kiel 24143, Germany

^k Department of Microsystems Engineering, University of Freiburg, Freiburg 79085, Germany

ARTICLE INFO

Keywords:

Cooperative microactuator systems
Bistability
Multistability
Metastable energy systems
Microtechnology
MEMS

ABSTRACT

The smart coupling of microactuators to cooperative microactuator systems enables new functionalities like active bi- and multistability requiring no external force for switching between stable states. This review explores different concepts of cooperative microactuator systems combining microactuation based on either the same or different transducer principles. The transducer principles comprise electrostatic, magnetic, dielectric elastomer and shape memory effects as well as combinations thereof. Thereby, active bi-/multistable switching is achieved via selective control of the microactuators using diverse control signals based on thermal, electrical or magnetic stimuli. The combination of the microactuators in confined space gives rise to various coupling effects and cross-sensitivities that need to be considered. In the following, the engineering aspects of material properties, microsystems design and fabrication, as well as experimental and numerical characterization of system performances and dependencies on design parameters will be discussed. The presented microactuator systems will be assessed with respect to their energy characteristics and critical forces for switching. Their application potential will be highlighted.

1. Introduction

Miniaturization and increase of functionality are global trends in various fields of engineering and technology. As a consequence, novel smart devices and systems are being developed with increasing complexity comprising various sensors and actuators. Typical examples are lab-on-chip systems [1,2], RF MEMS devices [3] or optical mirror devices like the well-known digital mirror device containing millions of microactuators [4]. The development of actuators at different length

scales strongly depends on materials and corresponding technologies. Silicon is the key material in microelectronics technology, but it is not a transducer material. Therefore, additional suitable materials need to be introduced to enable actuation, like metal or magnetic layers, piezoelectric or shape memory alloy (SMA) films. Up to now, various microactuators have been developed based on the integration and micromachining of different transducer materials. For recent reviews the reader is referred to [5–7]. Today, microactuators are in most cases single components, either integrated into systems, such as electrostatic

* Corresponding author.

E-mail address: manfred.kohl@kit.edu (M. Kohl).

<https://doi.org/10.1016/j.snr.2025.100338>

Received 27 November 2024; Received in revised form 11 April 2025; Accepted 8 May 2025

Available online 11 May 2025

2666-0539/© 2025 The Authors. Published by Elsevier B.V. This is an open access article under the CC BY license (<http://creativecommons.org/licenses/by/4.0/>).

actuators in gyroscopes or scanning mirrors, or assembled into systems, such as micropumps in fluidic networks. Only few examples exist, where several millions of them are arranged in microactuator arrays like the digital mirror device consisting of many identical, though individual actuators that operate independently from each other. Cooperative microactuator systems are envisioned as a new generation of devices that use the synergy of different microactuators in order to enable enhanced system properties like multifunctionality, multistability and multistage performance. However, the emerging field of cooperative microactuator systems is still in its infancy [8,9]. It will be important to identify and systematically explore the synergy effects in cooperative microactuator systems and, at the same time, to understand and control the various coupling effects caused by the close vicinity of many transducer materials and functional structures.

Bistable and multistable systems are characterized by two or more stable states separated by energy barriers. These systems have a large potential to save energy, since energy is only required when switching between the states. Each stable state represents a condition where internal forces cancel each other out, bringing the system to a force equilibrium condition. The transition between these states occurs when an external stimulus disrupts the force equilibrium, leading to a controlled release of stored energy. The energy barrier plays a pivotal role in governing the stability and dynamics of the system, providing a critical threshold that must be overcome to transition between the stable states. Notably, the energy barrier that separates the stable states corresponds to the minimum energy required for the transition. Understanding and manipulating the energy barrier is fundamental to the design and optimization of bi-/multistability in various applications.

At the macroscale, bi- and multistable mechanisms have been explored extensively [10,11]. Generally, switching between stable states is accomplished either by overcoming the energy barrier by applying a sufficiently large external force or by actively changing the energy landscape itself. In the first case, the energy landscape is generated by passive compliant structures requiring external actuation to switch between the stable states [12,13]. At the miniature-scale, this approach has been pursued, e.g., in the development of clamped membranes that can switch between two stable out-of-plane deflection states [14–16].

Upon further miniaturization to the microscale, the second approach of actively controlling energy levels is of special interest due to size constraints. Therefore, external actuators should be replaced by integrated actuation concepts. Following this approach, magneto-static latching has been explored [17,18]. By integration of ferromagnetic layers and miniature-scale permanent magnetic structures, bistable switches and bistable microvalves have been introduced [19,20]. Novel bistable actuators have been developed making use of an extended range of stimuli including electrical [21,22], magnetic [23,24] and thermal fields [25]. The use of smart materials such as shape memory [26,27] and piezoelectric materials [28,29] has led to the development of bistable mechanisms that no longer rely on an external load but utilize their intrinsic transducer properties to induce bistability. Compact systems with active bistability have been realized, e.g., by designing compliant shape memory alloy (SMA) film structures that switch between stable states by inducing the shape recovery force of the SMA film upon heating [30].

In the following, we present selected concepts of cooperative microactuator systems to generate active bi- and multistability. These concepts comprise different transducer materials and system architectures covering electrostatic, magnetic, dielectric elastomer and SMA principles, which enables various actuation mechanisms requiring dedicated microtechnologies for fabrication. Obviously, each concept has its own development environment and the characterization of system properties involves specific design parameters. Nevertheless, the different microactuator systems have in common that they all exhibit an energy landscape consisting of minima and energy barriers requiring critical forces to overcome. Therefore, this paper aims to assess the concepts of cooperative microactuators in terms of energy

characteristics and critical forces taking into account system dimensions. After a brief overview, each concept will be introduced and discussed with respect to energy and force characteristics as well as the governing design parameters to achieve bi- and multistability. This will allow for a direct comparison of the concepts with respect to energy barrier heights and critical forces as well as overall size.

2. Overview of concepts

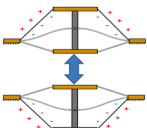
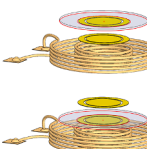
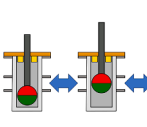
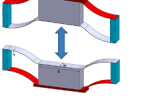
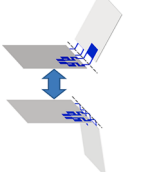

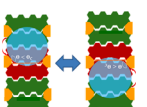
Table 2.1 provides an overview of the concepts of cooperative microactuator systems presented in this review. Section 3 considers two cone-shaped DE actuators coupled with a bistable polymeric biasing element. In this case, electrostatic actuation is used for switching between stable positions. A hybrid levitation microactuator is presented in Section 4, which combines electromagnetic inductive and electrostatic actuation. A proof mass is magnetically levitated using a two-coil configuration within the static electric field of a top and bottom electrode. The linear stiffness of the electromagnetic suspension is tunable by the electric field in a wide range. In particular, bistable behavior is observed by applying a critical pull-in voltage to either the top or bottom electrode, at which the stiffness becomes zero and the proof mass jumps towards either the electrodes. The nonlinearity of magnetic fields is used in Section 5 to achieve multistability of a permanent magnetic plunger that can freely move in out-of-plane direction. The stable positions are tailored using multiple thin rings of steel. Switching between these positions is achieved by electromagnetic actuation.

In Section 6, a bistable microactuator is considered comprising two coupled SMA beams that are clamped at both ends and coupled in their center by a spacer. The SMA beams are designed to exhibit monostable behavior in heated (austenitic) state and to have different memory shapes being deflected in opposite out-of-plane directions. Thus, selective heating of the opposing monostable SMA beams induces bistable behavior. Following the concept of origami structures, bidirectional folding SMA microactuators are designed as an antagonistic pair in Section 7, whereby their memory shapes are adjusted to opposite bending states in out-of-plane direction. Selective heating of the folding actuators allows to switch between two end positions, which remain after actuation due to the metastable properties of martensite variants. A trilayer system consisting of a polymer, SMA and silicon is considered in Section 8. SMA-Si bilayer composites allow for bi-directional actuation due to the bimorph effect, which is amplified by the large strain change in the SMA layer during martensitic transformation. Compact bistable actuators can be achieved by adding a third layer of a polymer to such composites having a glass transition temperature that falls in between the martensite and austenite phase transformation temperatures. Depending on the maximum temperature upon heating, the polymer layer stabilizes either the deformation in martensitic or austenitic state. Section 9 considers a freely movable liquid droplet on a hydrophobic surface that is pinned by an electrode pair with a predefined gap. Bi- and multistability occurs by applying an electrostatic force on either the front or back electrode pair to override the surface tension allowing the droplet to pass the gaps in forward or backward direction.

The presented concepts comprise a wide range of actuation principles that are common to microsystems including electrostatic and dielectric elastomer effects, electromagnetic and shape memory effects. Bidirectional actuation can be obtained in antagonistic systems consisting of counteracting actuator pairs. Their actuation performance becomes bistable by combining them with a mechanically bistable membrane or a latching mechanism to introduce a biasing force with negative stiffness. Examples are presented in Sections 3, 6 and 7. Multistable actuation can be realized by the multiple use of the same actuation principle in an array of cooperating microactuators. Examples include stacks of thin ring-shaped magnets and steel plates (Section 5) and arrays of electrode pairs on a hydrophobic surface (Section 9). Another option to develop bi- and multistable systems is the combination of two different actuation principles, whereby one type of actuators

Table 2.1

Overview of concepts of cooperative microactuator systems to generate active bi- and multistability.

Sect.	Actuation principle	Layout	Bi-/multistable mechanism	Dimensions [mm ³]	Ref
3	Dielectric elastomer (DE) effect		Coupling of antagonistic monostable DE beams with a bistable polymer beam	50 x 3 x 5	[31,32]
4	Magnetic (Inductive Hybrid) levitation		Combined magnetic-electric force instability	10 x 10 x 2	[33–35]
5	Electromagnetic		Multiple magnetic latching within a stack of thin ring-shaped ferro-magnetic plates	11.5 x 11.5 x 10.5	[37,38]
6	Shape memory effect		Antagonism of coupled monostable SMA beams	10 x 1 x 2	[39]
7	Shape memory effect		Antagonism of coupled SMA cantilevers	10 x 22 x 0.14	[40,41]
8	Combined shape memory bimorph and glass transition effect		Fixation of shape memory bimorph deflection through polymer glass transition	1 x 0.015 x 0.023	[42–44]
9	Electrostatic		Multiple electrostatic force instability (n – number of electrodes)	1 x 1 x 2n	[45]

could be used, e.g., for switching and the other for fixation. One example is the combination of magnetic actuation for levitation and fixation of the position of a proof mass (Section 4), while electrostatic actuation is used for tuning the stiffness of the electromagnetic suspension and switching between stable states. Similarly, the bimorph shape memory effect can be used for switching between states in austenitic and martensitic state, while the fixation of the end position can be achieved by using the glass transition in an additional polymer layer (Section 8).

3. Bistable dielectric elastomer (DE) actuator

DEs are usually designed as actuators by either exploiting their in-plane deformation or by mechanically biasing a single membrane along a direction, which is usually chosen as perpendicular to the membrane plane. This describes a monostable actuator that can vary its one and only stable equilibrium point through electrical actuation. Existing literature reports their use for applications such as artificial muscles [46], haptics [47] and high-lift micro-aerial robotics [48], as well as in microactuators for tunable lenses [49], Braille displays [50] and positioning stages [51]. If the mechanical biasing system is designed in a suitable manner, the resulting actuator can be made bistable, and the transitioning between the equilibria can be controlled via an electric voltage input. Building on related previous works exploiting cooperativeness [31,52] and bistability [53], this section presents the

description and a static simulation study of such type of actuator.

3.1. Geometry and layout

A bistable DE actuator can be obtained starting from a pair of agonist DE membranes coated with conductive electrodes that are both pre-stretched over their planar directions and mechanically displaced orthogonally to their plane in opposite directions. A possible physical realization of such system is shown in Fig. 3.1 and consists of two cone DE membranes rigidly connected along the outer diameter, and pre-tensioned out-of-plane against each other via a rigid spacer. The centers of the membrane are subsequently connected with a bistable

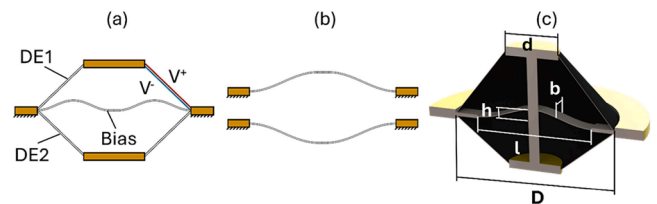


Fig. 3.1. Schematic layout of double cone DE actuators coupled with a bistable polymeric biasing element: (a) section view, (b) two stable states of a curved buckling beam, (c) cross-section layout of the bistable actuator with characteristic geometrical dimensions.

mechanical element, such as a pre-compressed beam exhibiting buckling instability, as shown in Fig. 3.1(b). This bistable element serves the purpose to increase the overall range of the actuator and can additionally make the overall system bistable. When a voltage is applied to either of the DE membranes, the central part displaces along its orthogonal direction, thus generating an out-of-plane stroke as can be seen in the actuation cycle of Fig. 3.2. By considering a fixed choice for the geometric parameters of the DE membranes, the resulting behavior (and, in turn, the bistability property) of the system is influenced by both geometrical parameters of the biasing system, such as length l , width b , and height-to-thickness ratio h/t , as well as material parameters. Here, PET is considered as a well-suited material for DE-based systems with characteristic dimensions in the mm range.

3.2. Actuation mechanism

When one of the DE membranes is electrically activated, the resulting Maxwell stress induces an equivalent in-plane softening within the membrane because of its stiffness being partially employed to counter-balance the electrical Coulomb forces. This causes the biasing system to overcome the forces exerted by the membrane until a new equilibrium state is achieved, thus resulting into a stroke. In stationary conditions, once the actuation voltage of a membrane reaches a threshold value, the system quickly displaces. During buckling, the system is only balanced by inertial and viscoelastic forces until it reaches the new stable equilibrium point. In dynamic applications, the bandwidth of typical DE actuators ranges from DC up to a few kHz [54], while actuation exploiting bi-stable buckling can be sustained up to driving frequencies on the order of 10^2 Hz [55]. Theoretical actuation efficiency values can reach up to 90% under optimal conditions [56], while experimental studies reported values of up to 60% when including charge recovery electronics and up to 18% otherwise [57]. Fig. 3.3 shows the static input-output behavior of a demonstrator system in terms of voltage applied to the membrane and relative displacement of the central point of the structure. Referring to the layout of Fig. 3.1(c) for the characteristic geometrical quantities, the simulated system considers a fixed DE geometry where the membrane has an external diameter $D = 5$ cm and an internal contact diameter $d = 2.44$ cm, both after a 10% pre-stretch. The membrane is $20 \mu\text{m}$ thick and the maximum applied voltage to each DE is 1.8 kV . The buckling beam is of length $l = 48.7$ mm, width $b = 4$ mm, thickness of 0.5 mm and out-of-plane pre-deflection $h = 6.8$ mm. Because of the existence of multiple equilibria in a working region of the system, its characteristic is fundamentally hysteretic. Additionally, due to the asymmetric force-displacement relation of buckling beams, the working range of the system is also asymmetric.

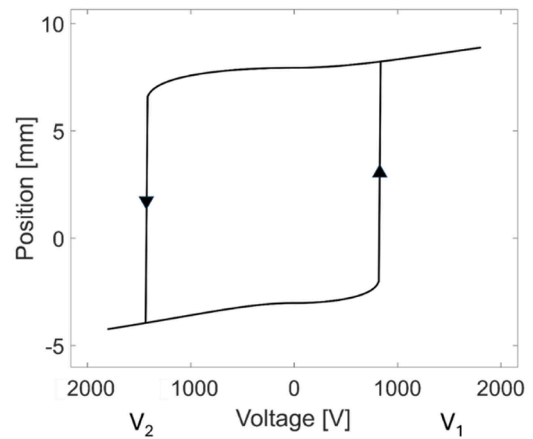


Fig. 3.3. Hysteretic actuation cycle of a bistable double cone DE actuator with direction of motion in the branches where bistability is affected. The geometric parameters of the DE membranes are: External diameter $D = 5$ cm, internal diameter $d = 2.44$ cm, thickness $t_m = 20 \mu\text{m}$. The geometrical parameters of the biasing system are: length $l = 48.7$ mm, width $b = 4$ mm, height-to-thickness ratio $h/t = 13.6$.

3.3. Force and energy results

Fig. 3.4(a) and (b) show, respectively, the matching between the forces of the biasing system and the total force of the double cone DE under different actuation voltage combinations, as well as the energy landscape of the resulting combined system under the same actuation conditions. It is readily observed that the shape of the bias curve allows for an overall system featuring two stable equilibria, represented by the two minima of the stored energy of the system without electrical actuation. When either of the two DE membranes is actuated, the stable equilibria gradually collapse in a single point, which is unique depending on which DE membrane is actuated. The system thus becomes monostable, presenting a single stable equilibrium also according to its energetic description. Switching from state A1 to state B1 via A2 requires a minimal switching force of about 350 mN , while the energy barrier to be overcome is about 2.85 mJ . Switching in opposite direction requires a higher switching force of about 970 mN and the corresponding barrier height is about 0.59 mJ . For the non-optimized geometric actuator design, the energy efficiency to switch to the opposite bistable position while causing the beam to buckle and store energy is approximately 20% while accounting for both electrical losses and viscoelasticity. During switching, a power input of at most 300 mW is required to perform the jump in 10 ms while as much as 240 mW are lost in damping forces and electrical losses.

3.4. Bistability region

The design of the biasing system requires careful tuning for its force-displacement characteristic to match the DE ones in the right way as to realize a normally bistable mechanism. It is well documented in the literature how a stress-free curved beam can be made monostable or bistable by changing geometric dimensions, such as the height-to-thickness ratio, or even boundary conditions [58]. In this setup, however, even a bistable bias can result in an overall monostable system, based on how the beam and the membrane forces add up. Fig. 3.5 shows the region in which, for a fixed DE membrane choice, the system is normally bistable normally monostable or electrical actuation does not lead the system to a desired monostable configuration. It should be noted, however, for a different choice of the DE setup, the region will

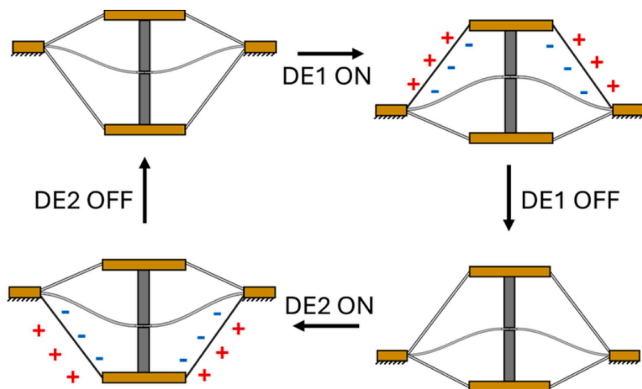


Fig. 3.2. Example of actuation cycle. From top left, clockwise: 1st stable state, actuation of DE1, deactivation of DE1 and 2nd stable state, actuation of DE2.

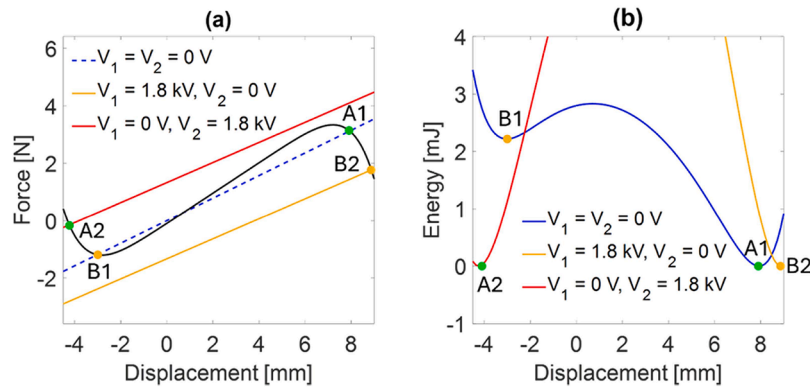


Fig. 3.4. (a) Force versus displacement curves of both biasing element (black), sum of the DE membrane forces under different voltage actuations (dashed blue, red and yellow) and relative points of equilibrium A1, A2 and B1, B2; (b) static stored energy landscape of the system described by summing all the forces of the components (b). The dimensions are the same as in Fig. 3.3.

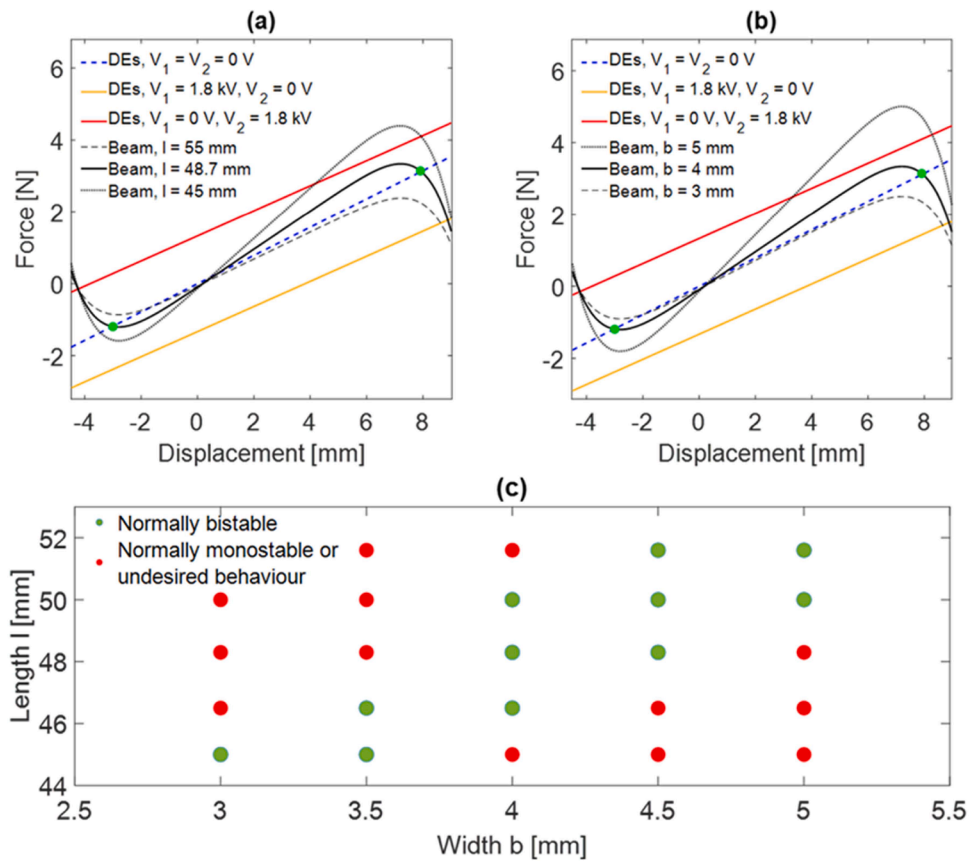


Fig. 3.5. Working regions of the system while varying length l (a) and width b (b) of the beam. The green dots represent the stable equilibria at low voltage for correct design choices of the beam (full black lines). The behavior of the system depending on the length and width of the stress-free curved biasing beam is summarized in (c).

look similar but with a slightly different shape depending on the magnitude of the forces in play.

4. Bistable inductive levitation microactuator

A hybrid levitation microactuator implemented by means of combining electromagnetic inductive and electrostatic actuation demonstrates dramatically increased operational capabilities, such as dynamic tuning of the stiffness components, linear and angular positioning of a proof mass (PM) with adjustable dynamics, as well as operation as the bistable micro-actuator [33,59–65]. Early concepts of magnetic

levitation can be found, e.g., in [66]. The advanced application of such actuators requires the comprehensive study of the pull-in phenomena, which finally defines their operating regimes [59,65,67,68]. In particular, the linear pull-in actuation in the bistable inductive levitation micro-actuators is discussed. The effect of the design parameters of the device on its actuation mechanism, which is characterized by its force and energy performance, is analysed below.

4.1. Geometry and layout

The layout of the bistable inductive levitation microactuator is

shown in Fig. 4.1. A typical two-coil configuration, consisting of stabilization and levitation one, arranged to provide stable levitation of a conducting disc-shaped PM, is considered. Worth noting that a PM having other shapes such as square, pentagon, hexagon one can be also stably levitated by this coil configuration [69]. The PM is magnetically levitated within the static electric field generated by the top and bottom electrodes. In the general case, it is assumed that the potentials that are applied to the top and bottom electrodes are different and denoted by u_1 and u_2 , respectively, as shown in Fig. 4.1. The equilibrium point coincides with the origin O , which lies on the y axis of symmetry. The location of the origin is characterized by the following parameters: h is the spacing between the bottom electrode plane and the origin, h_l is the levitation height, which is estimated as the distance between the planes formed by the upper turn of the coils and the origin (The point C is lying on the crossing of the y axis and the upper turn coil plane). The displacement of PM is characterized by the generalized coordinate y . The mass of PM is denoted by m . The radius of PM, r_{pm} , is larger than the radius of the levitation coil, r_l , but less than the stabilization one, r_s . Hence, the following inequality $r_s > r_{pm} > r_l$ holds.

It is assumed that the PM is levitated stably between the top and bottom electrode pairs at the middle. Also, the area of each electrode is the same and denoted by A_E . For further discussion, the set of dimensionless parameters is introduced. Namely, $\kappa = h/h_l$ is the spacing parameter, which characterizes the distance between the electrode pairs and the PM. $\beta_i = \varepsilon_0 A_E u_i^2 / (mgh^2)$, $i = 1, 2$, is the dimensionless square voltage, where ε_0 is the permeability of free space and g is the gravitational acceleration. $\xi = 0.5h_l/r_l$ is the design parameter and $\lambda = y/h$ is the dimensionless displacement of the PM. Worth noting that, for all known micro-fabricated prototypes of actuators published in the literature, the parameter ξ is less than 0.25. The micromachining prototype of such an actuator was first reported in [34]. The prototype is characterized by the following parameters: the weight, mg , is $3.7 \mu\text{N}$; the levitation height, h_l , is $150 \mu\text{m}$; the spacing, h , is $100 \mu\text{m}$; the radius of the levitation coil, r_l , is 1 mm . Hence, the dimensionless parameters are $\kappa = 0.666$ and $\xi = 0.075$.

4.2. Actuation mechanism

Two operation modes of the actuator according to subsequences of energizing the electrode pairs can be recognized. Namely, operation mode I is characterized by energizing the top or bottom electrode pair separately, while in operation mode II both electrode pairs are energized simultaneously.

The bistable actuation mechanism performed in operation mode I is as follows. Energizing either the top or bottom electrode pair selectively

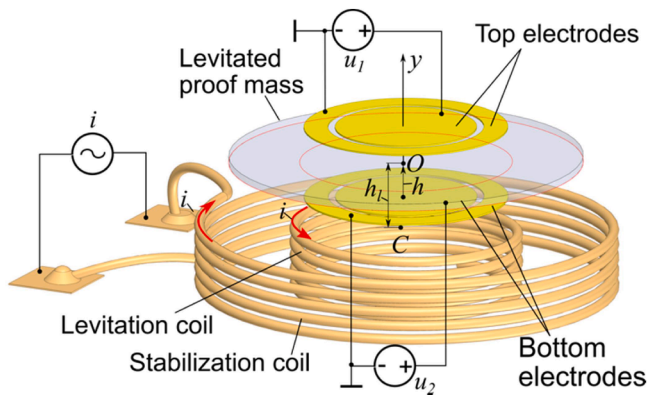


Fig. 4.1. Schematic layout of the bistable inductive levitation microactuator: i is the AC electric current; u_1 and u_2 are applied voltages to the electrodes; h is the spacing between the bottom electrode plane and the origin O ; h_l is the levitation height estimated from the plane of the upper turn of the coils.

generates the electrostatic force, which moves the PM toward to the energized pair. Simultaneously, the electric field produces the negative stiffness reducing the stiffness of the magnetic suspension. Upon applying a certain value of the voltage to the electrode pair the resultant stiffness becomes zero. Note that the voltage and the displacement of PM corresponding to this state are called the pull-in voltage and the pull-in displacement, respectively. Hence, when the pull-in voltage is applied to the electrodes, PM moves to the electrodes in a jump. Once the voltage is released, PM resets to its origin by means of gravity and the electro-magnetic force.

The general behavior of operation mode II is studied in [70,71]. Here, we consider the particular case that both electrode pairs are energized by the same voltage $u_1 = u_2 = u$ [35]. In this mode, the linear stiffness of the electromagnetic suspension at the equilibrium point can be adjusted in a wide range or completely eliminated by controlling the strength of electric field. Once the pull-in voltage is applied to the electrodes and the stiffness becomes zero, PM moves from its origin to the top electrodes in a jump. Subsequently, PM experiences monostable behavior shifting below the origin. Upon eliminating the stiffness by applying the second pull-in voltage, PM moves toward the bottom electrode pair in a jump.

4.3. Force and energy results

The force- and energy-displacement curves and their evolutions depending on the square voltage β are shown in Fig. 4.2 for operation mode I. In particular, Fig. 4.2(a) presents the dimensionless force-displacement curves for the square voltage β_1 in a range from 0 to 0.5 and β_2 in a range from 0.4 to 0.7. The design of the actuator is characterized by the following parameters, namely, $\kappa = 1.0$ and $\xi = 0.2$. The dimensionless force \bar{F} is represented as the ratio of the resulting electromagnetic force acting on the PM to its weight. An analysis of Fig. 4.2 indicates that the PM has one stable equilibrium point at $\lambda = 0$ when the electrodes are uncharged ($\beta_1 = 0$). Hence, the electromagnetic force acting on the PM increases monotonically in the negative displacement range and decreases in the positive one. The dimensionless energy-displacement curve exhibits a minimum for $\beta_1 = 0$ corresponding to a stable state as shown in Fig. 4.2(b).

When the top pair of electrodes is energized and the applied voltage β_1 is less than the pull-in one, then the force has two equilibrium points, S_i^+ and U_i^+ , which satisfies the stable and unstable states, respectively. The energy curves have the corresponding minimum and maximum value, respectively, as seen in Fig. 4.2(b). Due to the fact that electromagnetic force generated by the electric current in the coils is decreased, the force curves have the minimum values between the points S_i^+ and U_i^+ . Then the equilibrium points are merged into the bifurcation point B_1 , when the applied voltage reaches the pull-in one as shown in Fig. 4.2 (a,b). Beyond the pull-in voltage, the actuator has no equilibrium state and moves toward the energized electrodes. Similar to the positive range of displacement, the actuator experiences the bistable mechanism in the negative range of displacement, when the bottom pair of electrodes is energized. The only difference is that the force curves have maximum values between two equilibrium points S_i^- and U_i^- , due to the increasing value of the electromagnetic force.

Note that to convert the dimensionless force and energy into corresponding units, the following equations can be used, namely, for electromagnetic force, $F = mg\bar{F}$ and for energy, $E = mgh\bar{E}$. As an illustrative example let us consider the prototype having parameters mentioned above, but it is assumed that $h_l = h = 400 \mu\text{m}$ to fit the requirement for $\xi = 0.2$. Hence, the maximum electromagnetic force acting on the PM for negative range of displacement becomes $F_{\max} = 3.7 \cdot 2.176 = 8.0512 \mu\text{N}$ ($\beta_2 = 0.4$) and the energy barrier for bistable actuation in the negative range is $E_B = 3.7 \cdot 400 \cdot 10^{-6} \cdot 1.5651 = 0.0023 \mu\text{J}$ ($\beta_2 = 0.608$) (see Fig. 4.2). For positive range of displacement, we can write $F_{\min} = 1.0 \mu\text{N}$ ($\beta_2 = 0.09$) and $E_B = 7 \cdot 10^{-4} \mu\text{J}$ ($\beta_1 = 0.215$) (see Fig. 4.2). The

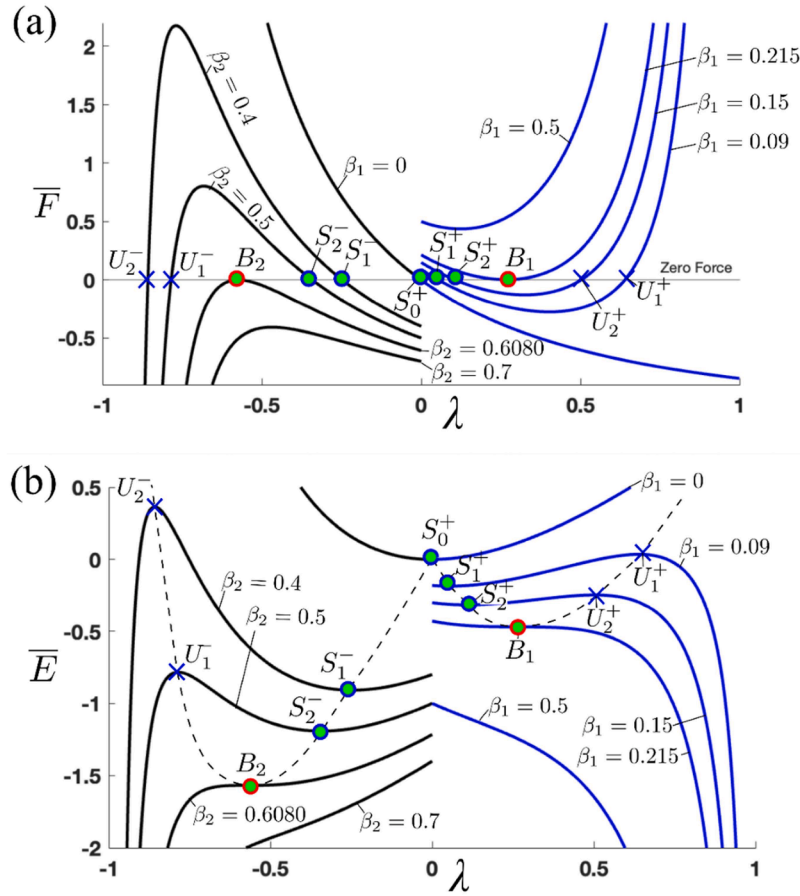


Fig. 4.2. (a) Force-displacement, (b) energy-displacement of the bistable system: B_1 and B_2 are the bifurcation points for the positive and negative range of displacement, respectively; S_i^+ and S_i^- ($i = 0, 1, 2$) are the stable equilibrium points for the positive and negative range of displacement, respectively; U_i^+ and U_i^- ($i = 1, 2$) are the unstable equilibrium points.

energy barrier can be decreased by decreasing the spacing parameter and locating the electrodes closer to the PM, for instance, if $\kappa = 0.1$ then $E_B = 7.4 \cdot 10^{-6}$ μJ for both ranges of displacement.

4.4. Bistability region

The regions of monostable and the bistable behavior of the actuator for both operation modes are presented in bifurcation diagrams shown in Fig. 4.3. The diagrams are built for different design parameters κ and ξ in terms of the dimensionless voltage and displacement. They map the distribution of centre and saddle points characterized stable and unstable equilibrium state, respectively, as well as show the bifurcation points where the bistable actuation occurs.

For operation mode I, the bifurcation diagrams for the actuator characterized by the following design parameters, namely, $\kappa = 1.0$ and $\xi = 0.2$ are shown in Fig. 4.3(a). As seen from the figure, monostable actuation is limited by the bifurcation points B_1^+ and B_1^- in positive and negative range of the displacement, respectively. These two points are defined by the pull-in voltages ($\sqrt{\beta_1^+}$ and $\sqrt{\beta_1^-}$) and pull-in displacements (λ_1^+ and λ_1^-), where the actuator experiences bistable actuation. The pull-in voltage for negative range is larger than for positive one ($\sqrt{\beta_1^-} > \sqrt{\beta_1^+}$). Also, the range of displacement for monostable actuation in the negative range of displacement is larger than for the positive one ($\lambda_1^- > \lambda_1^+$). Decreasing the spacing parameter κ leads to decreasing in the range of displacement for monostable actuation and its pull-in voltages, see Fig. 4.3(a). In a particular case, when κ tends to zero, the pull-in displacement has the tendency to be $\lambda^+ = \lambda^- \approx 1/3$ for both ranges, as well as the pull-in voltage, which can be approximately estimated as

follows: $\sqrt{\beta^-} = \sqrt{\beta^+} \approx \sqrt{\kappa 4/27(1 + 1/[\ln 4/\xi + 2])}$.

For operation mode II, the actuator having the following design parameters, namely, $\kappa = 1.0$ and $\xi = 0.07$ are considered. Its bifurcation diagrams are depicted in Fig. 4.3(b). As seen from the figure, there are two bifurcation points B_1 and B_2 . The PM keeps the original position till the pull-in voltage determined by the point B_1 in the diagram is applied to the electrodes. Beyond this point the actuator experiences the monostable regime limited by the second bifurcation point B_2 . Similar to operation mode I, decreasing the spacing parameter κ leads to decreasing in the range of displacement for monostable actuation and its pull-in voltages as well, see Fig. 4.3(b). Once κ tends to zero, two bifurcation points merge into one point as shown in Fig. 4.3(b).

4.5. Dynamic actuator performance

The inductive levitation microactuator can be executed in both, bistable and monostable, operation mode with high performance. Thereby, the time for bistable switching can vary in a wide range from milli to nano seconds, which can be adjusted through design parameters such as the spacing parameter κ , the applied actuation voltage $\sqrt{\beta}$ and friction reduction via controlled vacuum. Its energy and power performance can be significantly enhanced by carefully designing the micro-actuator's geometry, materials, and excitation strategies, for instance, by reducing the coil diameter [72] and incorporating a magnetic core in the coils [73]. The energy efficiency of pull-in actuation from the origin to one of the electrode pairs can be estimated by the dimensionless energy values associated with the bifurcation points, namely, B_1 and B_2 (see Fig. 4.2(b)). For the considered design, the energy efficiency of the

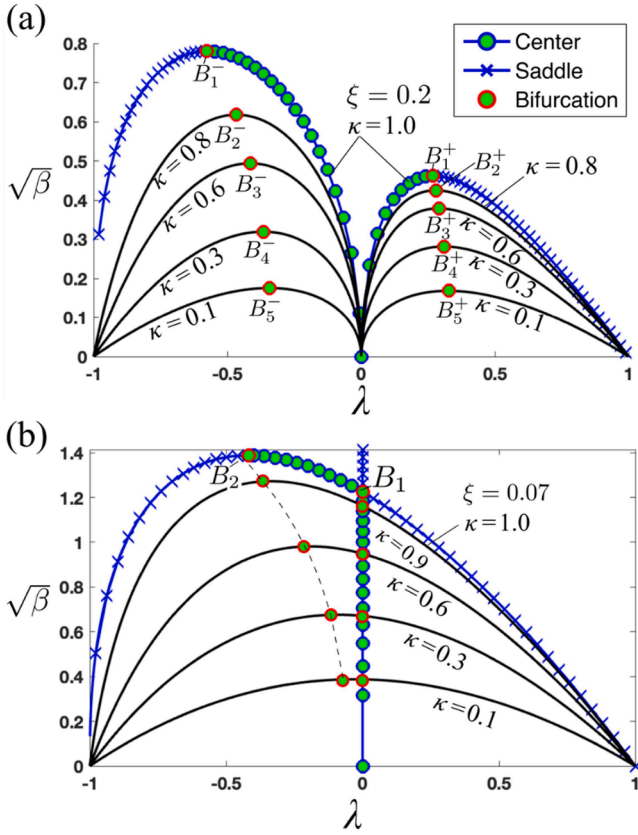


Fig. 4.3. Bistable and monostable regions: (a) bifurcation diagram for the operation mode I; (b) bifurcation diagram for the operation mode II ($u_1 = u_2 = u$).

pull-in actuation towards the top pair of electrodes is around 0.7, while towards the bottom pair it is around 0.4. The power efficiency of this design is estimated to be 0.9 as reported in [74]. This makes the proposed actuator concept well-suited for applications requiring low-power and high-precision actuation, such as the precise and energy-efficient cooperative movement of components in micro-robotic systems. The demonstrated bistable actuation can be utilized in MEMS-based optical systems including tunable lenses and beam-steering mirrors. Additionally, the proposed microactuator can enhance the performance of micro-inertial sensors through incorporating tunable stiffness and bistability.

5. Multistable magnetic lift actuator

Magnetic actuators are accessible, fast, and allow for contactless actuation, e.g., for levitation [71,75]. However, these devices continuously consume energy. As an alternative, the nonlinearity of magnetic fields can be exploited to design multistable actuators. Applications for multistable magnetic actuators include bistable magnetic switches [76], energy harvesters [77], multistable valves, [78,79] and grippers [80]. In general, these concepts are based on a movable, magnetic object that can be kept in a stable position in the vicinity of a permanent magnet. With an increased number of permanent magnets, more resting positions are achievable. However, only few miniaturized or microsystems with more than two stable positions have been investigated. An example of an actuator showing three resting positions is presented in [81]. In the following, we describe an actuator concept with so far three stable resting positions providing explicitly the potential for an arbitrary number of equilibrium positions. Here, a permanent magnetic plunger that can freely move in an out-of-plane direction is kept stable by multiple thin steel rings in the outer actuator structure. Varying their

vertical position shapes the energy barriers and allows to tailor the stable positions [36]. Additional stable positions might occur at the limits of the plunger's motion: if the total vertical force at such a position pushes the plunger against the limiting object, mechanical contact introduces another stable position. This work investigates how the steel rings' positions affect the magnetic force and the energy potential with respect to the displacement. The actuator is specifically designed for flexible reconfigurability and the possibility of creating additional stable positions. Switching between these positions is achieved by electromagnetic actuation. The actuation coil further provides the advantage to be also useful for self-sensing of the plunger position similar to [82], which is the basis for feedback control. Note that in contrast to other typical miniaturized magnetic systems [83,84], the magnetic actuation is included in the design and not supplied by external magnetic fields.

5.1. Geometry and layout

The basic components of the setup are the magnetic plunger, which consists of a spherical neodymium magnet (3 mm diameter) and a ferrite rod (7.5 mm length, 0.75 mm diameter), three thin steel rings (20 μ m thickness) for shaping the energy barriers, and a coil (3 mm diameter, 1 mm length) for electromagnetic actuation, see Fig. 5.1. The plunger is guided by both, the guiding structure at the base of the setup, and the Teflon bearing within the circuit board at the top. The actuation coil is wound around the Teflon bearing enclosing the ferrite rod. Stacks of phenolic paper are used as spacers to adjust the vertical position of the steel rings, and therefore also the resting positions of the plunger. Depending on the position of these rings, there are up to three resting positions: the upper and bottom positions, where the plunger is in contact with either the bearing or the base structure, and the middle position, in which the plunger is kept by an equilibrium of frictional, gravitational, and permanent magnetic forces.

5.2. Actuation mechanism and performance

To switch between the different stable positions, short electric current pulses are applied to the actuation coil. Due to the use of a permanent magnet, the plunger can either be pulled upwards or pushed downwards, depending on the sign of the input current. The amplitudes and lengths of the input signals are chosen based on the starting and desired final position, since less current is needed for a transition into the middle position, or when switching from a higher to a lower position, as we do not have to work against gravity. In general, more efficient and robust actuation signals can be found by model-based feedforward control, as presented in [85]. This is achieved by parameterizing the input current and using simulation-based, numerical optimization. Suitable dynamic models for simulation can be obtained using finite element modeling and subsequent techniques for model order reduction as in [86–88].

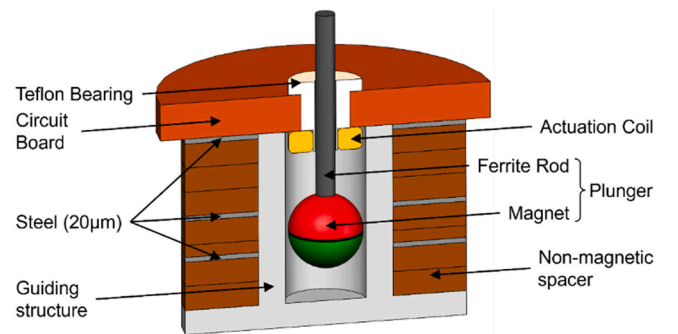


Fig. 5.1. Design of the multistable actuator with a freely moving, magnetic plunger [36]. Three stable resting positions are achieved by steel rings and contact with the base structure.

The frequency of actuation can be extracted from the transient position measurements [36]. Transition times between stable positions range from 20 ms to 40 ms for downward and upward transitions, respectively. Therefore, the actuator achieves a frequency of ca. 25 Hz. However, successive actuation cycles heat up the coil and limit the operation time. Note that a larger coil increases actuation frequency and active cooling the number of consecutive cycles.

5.3. Force and energy results

The permanent magnetic force F_{pm} acting on the plunger depends on its vertical position z and the configuration of the steel rings. To achieve the resting position at the top of the actuator, i.e., in contact with the Teflon bearing, the position of the third steel ring is set to the maximum height $z_3 = 7$ mm, directly below the circuit board. In this section, we investigate the effect of the remaining steel rings' vertical positions z_1 and z_2 on the multistability of the actuator. The measured and simulated force- and energy-displacement characteristics are shown in Figs. 5.2 and 5.3, whereby Fig. 5.2(a,b) shows the results for the initial design with $z_1 = 2$ mm and $z_2 = 3.5$ mm. In this case, three energy minima are present at 1, 1.8 and 3.3 mm. The gravitational force causes a direction-dependent switching performance. The energy barriers in between the energy minima are determined to be 1.8 and 1.7 μ J in upward (+) direction, while they are 2.2 and 1.3 μ J in downward (-) direction. The corresponding switching forces are 1.3 and 1.6 mN in upward (+) direction (5.2 and 3.8 mN in downward (-) direction). Varying the two steel rings' positions changes these characteristics. This can be used to adjust the middle resting position and to tune energy barriers. The number of stable positions as well as their origin may change, considering the force-displacement characteristic and mechanical contact. A FEM-based study investigates 91 design variations, varying the rings' positions between 0 mm and 6.5 mm in steps of 0.5 mm. Some variations occur twice as the two steel rings are interchangeable. In such a case, only one variation has been computed. Fig. 5.3(a,b) presents a subset of these 91 force- and energy-displacement characteristics, varying only one steel ring's position while the other is fixed at $z_1 = 0$ mm. We find for all values of z_2 at least one stable position. However, for some z_2 , we do not find an additional stable position at $z = 0$ mm, as the magnetic force overcomes the gravitational force. In contrast, for $z_2 = 1.5$ mm or 2 mm we observe a stable bottom position as the gravitational force exceeds the magnetic force. Similarly, only $z_2 = 4$ mm and 4.5 mm feature a stable top position.

The energy efficiency can be estimated from measurements of the coil current for transition and the force stroke characteristic [36]. The former is actuated for 32 ms with a constant current of 0.48 A. With a resistance of 14 Ω , the electrical work amounts to 0.1 J. The estimation of the mechanical work relies on the integrated force stroke curve, resulting in an energy stroke curve. For an energy barrier of 2.2 μ J, the efficiency is 2.2 μ J/0.1 J = 22 ppm. However, note that independent of

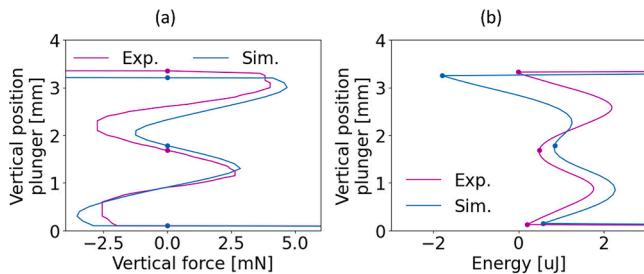


Fig. 5.2. Force-displacement and energy-displacement characteristics of the multistable actuator with highlighted stable positions: (a) measured and simulated results of the vertical force on the plunger for a single configuration ($z_1 = 2$ mm, $z_2 = 3.5$ mm); (b) corresponding potential energy characteristics; Lower and upper resting positions are achieved due to contact forces.

the duration, maintaining this position does not consume any further energy, even for moderate disturbances.

5.4. Multistability region

It has been demonstrated that the rings' positions are critical for the number and positions of the stable resting positions. In this section, we further investigate the parameter regions for which the design is mono-, bi-, or tristable. Based on the 91 force-displacement characteristics in the previous section, the number of stable positions and their composition can be derived.

These results are condensed into stability maps. Fig. 5.4(a) provides the total result, emphasizing the mono-, bi-, or tristability offered by the design space. Fig. 5.4(b) focuses on purely magnetic contribution, while Fig. 5.4(c,d) are dedicated to stable top and bottom positions due to mechanical contact, respectively. To design an actuator with the desired number and location of stable resting positions, an approach similar to [38] may be used: By superimposing the force contribution of a single steel foil on the plunger, a rough estimate of the overall force-displacement characteristic can be obtained. This concept has also been validated for a macroscopic setup using patterns of cylindrical magnets [89]. Numerical optimization can then find the required steel foil positions by minimizing the deviation between the approximated and desired force characteristic. It should be mentioned, however, that intermediate resting positions may not be reached without a more complex actuation mechanism, such as robust feedforward or feedback control. In [38], the dynamic transition between the stable positions at different weights of the plunger was investigated for a given configuration. It was shown that an additional weight of 70 mg on top of the initial plunger weight of 126 mg still resulted in three resting positions. However, no trivial actuation signal achieved a direct transition from the top position to the middle position without an undesired, large undershoot to the bottom position and a subsequent rebound.

6. Antagonistic bistable SMA beam actuator

The combination of SMA beams allows for the development of antagonistic SMA beam actuators that exhibit bidirectional deflection as well as active bistability [39]. In order to understand the complex thermo-mechanical performance of coupled SMA beams, a finite element investigation is conducted using a coupled thermomechanical SMA constitutive model developed in ABAQUS. In the following, we characterize the force-displacement and energy-displacement responses of single SMA beams with out-of-plane memory shapes in martensitic and austenitic states and, subsequently, the antagonistic coupling of two such SMA beams with oppositely deflected out-of-plane memory shapes, one being in martensitic and one in austenitic SMA state. Thereby, we analyze the influence of the major geometrical parameters on the bi-directional course of forces and energies versus displacement, namely the spacer length S and pre-deflection h , and explore the parameter range that supports bistable behavior. SMA actuators showing active bistability without the need for external loading offer great potential for switching applications at small scales such as microvalves, micro-positioning systems, microrobotic and biomedical devices owing to their ability to provide large actuation strokes and forces with stable mechanical states, along with their compatibility with microfabrication techniques and responsiveness to thermal stimuli [90–92].

6.1. Geometry and layout

The layout of the bistable actuator consists of two SMA beams with memory shapes being deflected in opposite out-of-plane directions. As sketched in Fig. 6.1, the SMA beams are coupled in their center by a spacer. The SMA beam ends are attached to two base parts made of a thermally insulating material. In addition, there are two heat sources placed at the top and bottom side of the coupled SMA beams. There are

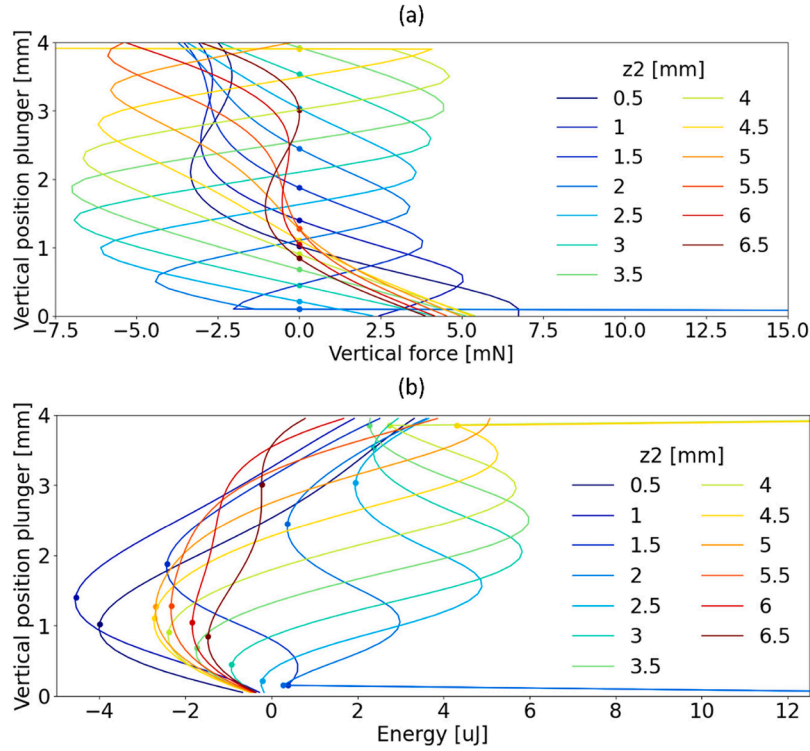


Fig. 5.3. Results of the numerical parameter study with highlighted stable positions: (a) simulated force-displacement characteristics for the lower ring fixed at $z_1 = 0$ mm and varying positions z_2 of the middle ring; (b) corresponding potential energy characteristics. Lower and upper resting positions are achieved due to contact forces.

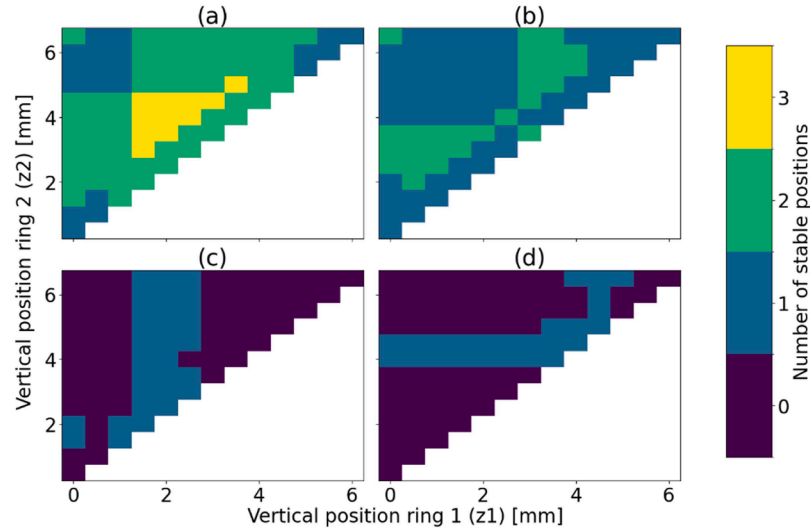


Fig. 5.4. Stability regions for mono-, bi-, and tristability with respect to the steel rings' positions considering the overall result as well as the contributions of individual effects. White area indicates symmetry as the two rings are interchangeable: (a) stability considering all effects; (b) stability due to the magnetic force-displacement characteristic; (c) stability due to a magnetic downwards force and mechanical contact at the bottom position; (d) stability due to a magnetic upwards force and mechanical contact at the top position.

seven geometrical parameters including L – beam length, w – beam width, t – beam thickness, r – bending radius near the spacer, R – bending radius at the beam ends, and h – initial out-of-plane deflection. Thereby, the length S and the deflection h as well as the bending radii r and R are considered as adjustable geometrical parameters. At low bending radius R , a straight section appears between the two curved sections. As the bending radius R increases, the length of this straight section decreases until it reaches to zero in the tangential limit of R_{tan} . In the simulation model, we assume the SMA material parameters of a $\text{Ti}_{53.9}\text{Ni}_{30.4}\text{Cu}_{15.7}$

film as described in literature [30]. The SMA beam thickness is $50\ \mu\text{m}$. The lateral beam dimensions are $10 \times 1\ \text{mm}^2$. Furthermore, the spacer height is $2\ \text{mm}$ to ensure sufficient thermal insulation between the SMA beams.

6.2. Actuation mechanism

Selective heating of the SMA beams is performed by solid-solid contact between the SMA beams and planar heat sources centrally

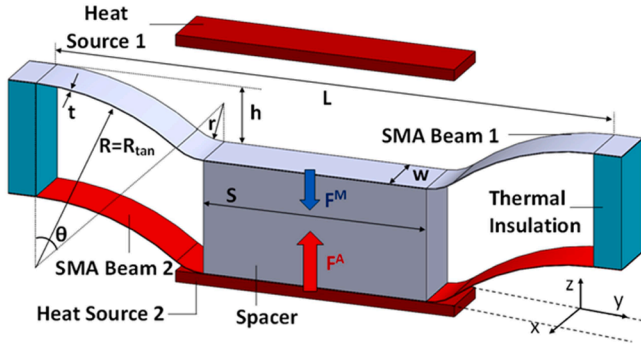


Fig. 6.1. Schematic layout of the bistable actuator consisting of two antagonistically coupled SMA beams that are clamped at both ends and deflected out-of-plane in the beam center. F^M and F^A denote the opposing forces of the SMA beams, one being in austenitic and one being in martensitic state. The geometrical parameters are introduced in the text; adapted from [39].

located at the top and bottom side of the SMA beams. Fig. 6.1 shows one of the stable equilibrium positions, in which SMA beam 1 is in its memory shape, while SMA beam 2 is deflected downwards in opposite out-of-plane direction compared to its memory shape. While in contact with heat source 2, the temperature of SMA beam 2 increases until it reaches the temperature range of martensite-austenite phase transformation, in which the memory shape begins to recover. The shape recovery force F^{A2} pushes SMA beam 1, which is still in martensitic state, upwards whereby it causes an opposing force F^{M1} . At sufficiently large displacement in z -direction, a dynamic snapping motion occurs driving the system towards the upper stable equilibrium position. Alternating heating of the antagonistic SMA beams causes bi-directional self-actuation of the actuator between two stable positions without the need for an external force. This mechanism suggests that the coupling force $F^{C2} = F^{A2} \cdot F^{M1}$ should be positive in the entire displacement range to

obtain bistable behavior of the antagonistic SMA beams. A similar criterion exists for the downward motion after selectively heating SMA beam 1. Since the force direction of the martensitic SMA beam is opposite of the austenitic one, the force of this beam is subtracted from the shape recovery force to calculate the coupling force. As the energy considerations are independent of direction, the energies of austenite (E^{A2}) and martensite (E^{M1}) are added to calculate total coupling energy of the system. Given that the proposed coupling energy (E^{C2}) is exactly corresponding to the defined coupling force (F^{C2}), it is concluded that for the bistable antagonistic system, the coupling energy should have only one minimum corresponding to the only one zero value of coupling force.

6.3. Force and energy results

The bistability of the antagonistic SMA beam actuator is investigated based on the force and energy characteristics of the SMA beam in austenite and martensite state. Fig. 6.2(a,b) shows the effect of spacer length S on the displacement characteristics in positive ($+z$) direction of coupling force $F^{C2} = F^{A2} \cdot F^{M1}$ and coupling energy $E^{C2} = E^{A2} + E^{M1}$, in which the actuator starts from an initial position near zero displacement with SMA beams 1 and 2 being in martensitic and austenitic, respectively. Based on the criterion of positive coupling force F^{C2} , it is concluded that bistable behavior of the antagonistic beam actuator is obtained only for spacer lengths S of 4 and 5 mm. For smaller and larger spacer lengths, i.e. $S = 3$ mm and $S = 6$ mm, F^{C2} becomes zero at intermediate positions causing the actuator to stop moving before reaching the equilibrium position (stable state 1). Similarly, moving from an initial position near maximum displacement in negative displacement direction towards stable state 2 requires selective heating of SMA beam 1 to austenitic state, while SMA beam 2 is in martensitic state (not shown).

The force-displacement characteristics allow to determine energy efficiencies of actuation between stable positions. The work output of a

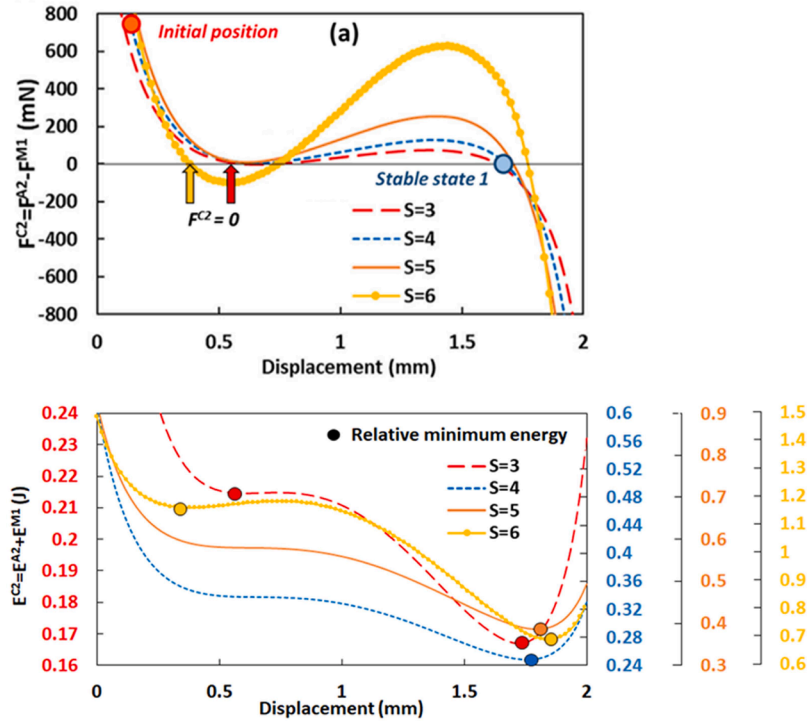


Fig. 6.2. The effect of spacer length S on the coupling force F^{C2} (a) and coupling energy E^{C2} (b) versus displacement in positive ($+z$) direction from initial position to stable state 1. The SMA beam geometries are $w = 1$ mm, $t = 50$ μ m, $L = 10$ mm, $h = 1$ mm, $r = 0.8$ mm and $R = R_{tan}$. Bistable switching behavior occurs when the coupling force F^{C2} stays positive in the entire displacement range. In this case, only one energy minimum occurs at zero force. Energy minima are indicated by colored circles.

single SMA beam actuator is in the order of 0.5 mJ. The heat input required to induced the phase transformation is estimated to be about 100 mJ for a TiNi-based alloy assuming typical values for heat capacity and transformation enthalpy [39,93]. The corresponding energy efficiency of 0.5% is rather low compared to non-thermal actuation mechanisms as most of the input energy is required to induce the phase transformation. The power input to induce phase transformation of a single SMA beam actuator within 0.5 s is about 200 mW, while the power output is in the order of 1 mW. Different approaches have been pursued to increase efficiency such as reducing the thermal mass while maintaining actuator stiffness and taking advantage of pulsed actuation [94]. Bistable actuation is another important concept to increase efficiency as power is only required for transitioning between the stable states. Generally, direct Joule heating of SMA actuators is mainly suitable at miniature scales, in which thermal masses are low.

Fig. 6.3 shows a finite element simulation of the force-displacement and energy-displacement characteristics of an antagonistic SMA beam actuator with spacer length S of 4 mm. Unlike the analysis of single SMA beams in austenite or martensite state and of their coupled performance in one loading step, the analysis of the fully coupled antagonistic SMA beam actuators requires two initial simulation steps to adjust the coupling of the two SMA beams and to reach one of the stable states as the starting position [39]. Active bistability occurs between the two stable states in upward (z increase, yellow line) and downward (z decrease, red line) direction, respectively. Switching between the two states is achieved as long as the minimal switching force between the stable states does not become zero. From Fig. 6.3, the minimal switching force is determined to be about 5.7 mN. The energy barrier depends on the displacement direction being about 95 mJ in upward (+ z) direction and 5.6 mJ in downward (- z) direction. The asymmetry between the energy states is caused by the initial conditions to adjust the coupling of

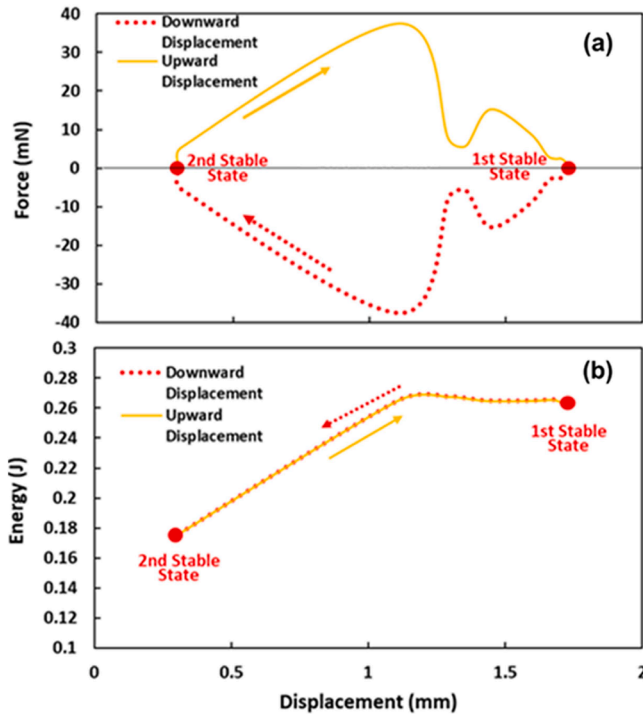


Fig. 6.3. Force versus displacement (a) and energy displacement (b) of an antagonistic bistable SMA beam actuator. The SMA beam geometries are $S = 4$ mm, $w = 1$ mm, $t = 50$ μ m, $L = 10$ mm, $h = 1$ mm, $r = 0.8$ mm and $R = R_{tan}$. Bistable switching between the two stable states occurs by crossing the energy barrier in between. The energy minimum of stable state 1 is higher than of 2 due to an asymmetry between the two states caused by the initial procedure to couple the two SMA beams; adapted from [39].

the two SMA beams for bistable actuation.

6.4. Bistability region

By performing FEM simulations for different geometries of antagonistic SMA beam actuators, we identify three distinct regions as shown in Fig. 6.4. There are two regions #1 and #2, in which the SMA beam actuator is monostable, and a bistable region. By increasing the spacer length S for a given pre-deflection h , the peak force of the opposing martensitic SMA beam strongly increases. Consequently, the required force of the austenitic SMA beam must increase as well to maintain bistability, which is no longer achievable at large S values. Conversely, reducing the spacer length S decreases the maximum stress of the SMA beam and, thus, the maximum force generated by the austenitic SMA beam eventually becomes insufficient. This analysis reveals that bistable behavior occurs at intermediate spacer lengths S for a given pre-deflection h . The bistability region can be characterized by defining the stability ratio SR , which is given by the ratio of R_{tan} (Fig. 6.1) and the bending radius of the beam center r ($SR = R_{tan}/r$). Then, the different bistable and monostable regions can be determined by the lower and upper limiting values SR_1 and SR_2 , respectively. For the investigated antagonistic SMA beam actuators, we find SR_1 and SR_2 to be 2.5 and 6.5, respectively. Their dependencies on geometrical parameters allow to determine critical values of predeflection h for the different monostable and bistable regions. As described in [39], we obtain two functions for the monostable regions #1 and #2, which are shown in Fig. 6.4 by red lines.

6.5. Dynamic actuator performance

The primary focus of this investigation is on the stationary performance of the antagonistic bistable SMA actuator, which is strongly affected by geometrical parameters. Under stationary conditions, the actuator performance can be predicted for applications at sufficiently low frequency when keeping stable positions over longer times. The cooling time required for transformation back to martensite depends on the thermal mass as well as the cooling mechanism of heat conduction as well as active/passive heat convection. If heat-induced switching occurs more rapidly compared to the cooling time, heat will accumulate and cause incomplete phase transformation, resulting in reduced or even loss of bistable performance. An interesting option, besides direct Joule heating of the SMA beams, is thermal actuation via direct solid-to-solid contact of the SMA beams with a low-temperature heat source. Dynamic measurements of thermally driven bistable SMA actuators using a heat source of 160 $^{\circ}$ C exhibit an oscillatory snap-through motion at frequencies up to 1.1 Hz due to periodic heating and cooling of the antagonistic SMA beams [30]. In this case, the time constants required for heating and for switching between equilibrium positions are determined to be 0.21 and 0.36 s, respectively.

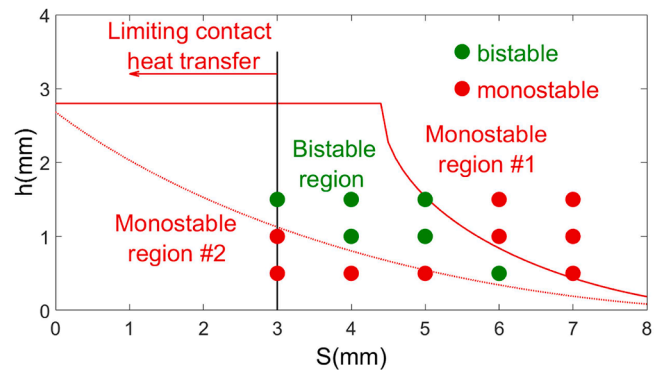


Fig. 6.4. Region of bistability and monostability of the antagonistic SMA beam actuator indicated in green and red colour, respectively [39].

7. Bistable SMA folding microactuator

Miniaturized folding actuators based on shape memory alloys (SMA) allow bending motion on mm and μm -scales enabling future applications of scalable origami-inspired structures [95–99]. Preliminary work has shown that miniaturized folding actuators based on SMAs have promising work densities and bidirectional folding behavior [40,41, 100–102]. Such devices may be designed as an antagonistic pair of SMA beams that exhibit an intrinsic bistability without the need for an external load to trigger the bistability. Bistable SMA folding microactuators could be used for handling of objects in microrobotics and micromanipulation in medical applications improving minimal invasive surgery. The microactuators could also be combined to novel origami-inspired re-programmable microsystems enabling applications, e.g., in smart surfaces, adaptive optics and photonics. The following sections present their concept, fabrication and the effect of design parameters.

7.1. Geometry and layout

The bistable SMA folding microactuator consists of two counteracting SMA double beams that connect two rigid tiles as illustrated in Fig. 7.1(a). The SMA beam structures are lithographically micro-fabricated from pre-annealed cold-rolled TiNi films having a thickness t of $20\text{ }\mu\text{m}$, while the tiles are laser-cut from polyimide. Both SMA double beams are heat-treated individually to adjust their memory shape at an angle of $\pm 180^\circ$. Subsequently, they are bonded to the tiles by hybrid integration using epoxy adhesives. The distance L between the tiles is $2000\text{ }\mu\text{m}$ and the intrinsic weight m of each tile is 97.5 mg . Cu-Sn microwires are electrically connected to the contact pads to power the SMA beams by Joule heating. SMA wing structures between the beam and pads increase temperature homogenization in the beam [103]. By selectively heating the antagonist and protagonist, the microactuator switches between two stable states as illustrated in Fig. 7.1(c,d). As illustrated in Fig. 7.1(b), the design parameters for tuning bistability include the SMA beam geometry as well as the shape-set angle θ_{ShapeSet} and tile mass m .

7.2. Actuation mechanism

The actuation in the SMA double beams is caused by the one-way shape memory effect, which is based on a martensitic phase transformation [104]. While in unheated condition, the microactuator is in planar state, whereby both SMA beams are undeflected and the

corresponding bending angle is 0° . By selective heating one of the counteracting SMA double beams above the austenitic transformation temperature, it deflects towards its memorized folded state and thereby deforms the opposing unheated SMA double beam. Consequently, the attached tile folds until it reaches its maximum folding angle Θ_{max} . Here, the torque of the protagonist being in austenitic state equals the torque of the antagonist being in martensitic state and the external load. After Joule heating and subsequent cooling to room temperature, the folding SMA microactuator relaxes and reaches the angle S_i , which is characterized by the meta-stable configuration of martensite variants of the SMA material. Depending on which of the two counteracting double beams is selectively heated, the maximum folding angle Θ_{max} , the meta-stable angle S_i and corresponding torque equilibria are reached in both, positive and negative, deflection directions. Thus, the SMA folding microactuator achieves bistability without the need for an external load. In this design, however, the maximum angle is limited by the torque balance [40,105]. In addition, asymmetries in deflection angles may occur due to fabrication tolerances. Therefore, an additional magnetic latching mechanism may be implemented to enhance the angular range and to stabilize the end positions [106].

7.3. Torque and energy barrier

The bistability of the SMA folding microactuator is investigated by simulating the bending of an individual SMA double beam with the geometry as defined in Section 7.1 in both martensitic and austenitic state. For this purpose, a finite element (FE) model has been developed to describe the coupled thermomechanical performance. Here, the model is used under isothermal conditions below the martensite finish and above the austenite finish temperatures. The FE code Abaqus Standard is applied, with a user-defined material library (UMAT) that includes the constitutonal thermomechanical behavior of the SMA material, as detailed in [107]. During the quasi-static simulations, kinematic control of the rigid top surface of the actuator is achieved by stepwise increasing its orientation angle from the shape-set initial position (here -180°) to the fully unfolded position ($+180^\circ$). The two bottom legs of the actuator are kept fixed, whereas all other degrees of freedom are allowed to relax in each step. The resulting torque to deform the structure for each discrete angle is determined as the reaction torque of the simulation step. The torque and energy of a coupled pair of antagonistic SMA actuators is derived from the combination of the simulated torque-angle response of the individual actuator at both austenite and martensite temperature.

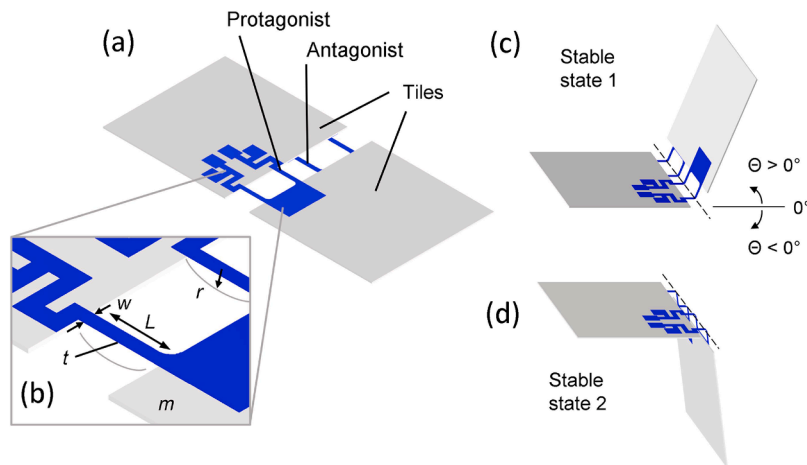


Fig. 7.1. (a) Layout of the bistable SMA folding microactuator consisting of two counteracting SMA double beams (protagonist and antagonist) that are bonded to rigid tiles. (b) Enlarged layout of an SMA double beam with tile mass m and geometric beam dimensions thickness t , width w , length L , and bending radius r . (c) First stable state triggered by the protagonist SMA double beam. (d) Second stable state triggered by the antagonist SMA double beam.

$$T_{\text{Coupled}} = T_{\text{Protagonist}-A} - T_{\text{Antagonist}-M} \quad (7.1)$$

By numerically integrating T_{Coupled} over the angle range, the coupling energy E_{Coupled} is calculated to investigate the bistability behavior of antagonistic SMA microactuators:

$$E_{\text{Coupled}} = E_{\text{Protagonist}-A} + E_{\text{Antagonist}-M} \quad (7.2)$$

Fig. 7.2(a,b) display the torque-angle characteristics of two individual SMA double beams with opposing bending directions and of the corresponding coupled beam system. Two metastable positions S_1 and S_2 are identified, at which the resulting torque of the protagonist and the antagonist microactuator becomes zero. The switching torque T_{sw} is determined from the increase of torque at the metastable positions when actuating the opposing SMA beam. In the present case, T_{sw} is determined to be about 8.7 N μm . The deflection of protagonist and antagonist versus temperature diagram in Fig. 7.2(c) shows a clear hysteresis with meta-stable points $S_{1,2}$ at room temperature. By integrating the torque over the angle, the energy of the coupled system is calculated, as illustrated in Fig. 7.2(d). It is observed that the energy minimum shifts between the positive and negative angular range, depending on which of the two counteracting double beams is selectively heated – protagonist or antagonist. The energy barrier is determined in the absence of heating by the energy difference at the intersection of the energy-angle characteristics at zero degree to be about 2.6 μJ .

The torque-angle characteristics allow to determine the energy efficiency to induce the bending motion. The mechanical work of a single SMA folding actuator is in the order of 20 to 45 μJ . In experiments we observe a complete phase transformation and corresponding termination of the folding motion after about 100 ms at an electrical DC pulse of 375 mW resulting in an electrical input energy of 37.5 mJ. The corresponding energy efficiency is 0.12%. Most of the electrical input energy is required to induce the phase transformation. Additional electrical

energy is consumed for heating the electrical contacts and the non-moving SMA parts of the microactuator. Therefore, bistable actuation is important to save energy as power is only required for switching between the stable positions.

7.4. Mono- and bistable behavior

Modifying the design parameters of the SMA folding microactuator affects its bistability behavior [108–110]. Fig. 7.3 shows a parametric simulation study comprising different bending radii of 100, 200 and 300 μm and film thicknesses of 5, 10 and 20 μm . It is evident that smaller bending radii result in elevated energy barriers as well as larger maximum angles and bistable angles. As visualized in Fig. 7.3(a), a barrier of 0.6 μJ and a maximum angle of about 100° are observed for a bending radius of 100 μm at a width of 300 μm and a thickness of 5 μm . Obviously, bistability is lost for a bending radius larger than 300 μm . For increasing thickness, the energy barrier increases while the angle shows a maximum at a beam thickness of 10 μm . In this case, an energy barrier of 1.9 μJ and an angle of about 130° are observed as shown in Fig. 7.3(b). At larger beam thickness, the energy barrier further increases to 2.6 μJ at a thickness of 20 μm and a bending radius and width of 100 μm , but the maximum angle decreases again to 60° due to the increasing stiffness of the antagonist beam. Below a thickness of 5 μm , no energy barrier exists and, thus, the system is not bistable. The angular range and bistability depend on external forces. The effect of an external weight on the maximum angle has been studied experimentally for actuation perpendicular to the gravitational field [41].

7.5. Dynamic actuator performance

The speed of bending motion depends on the heating power required

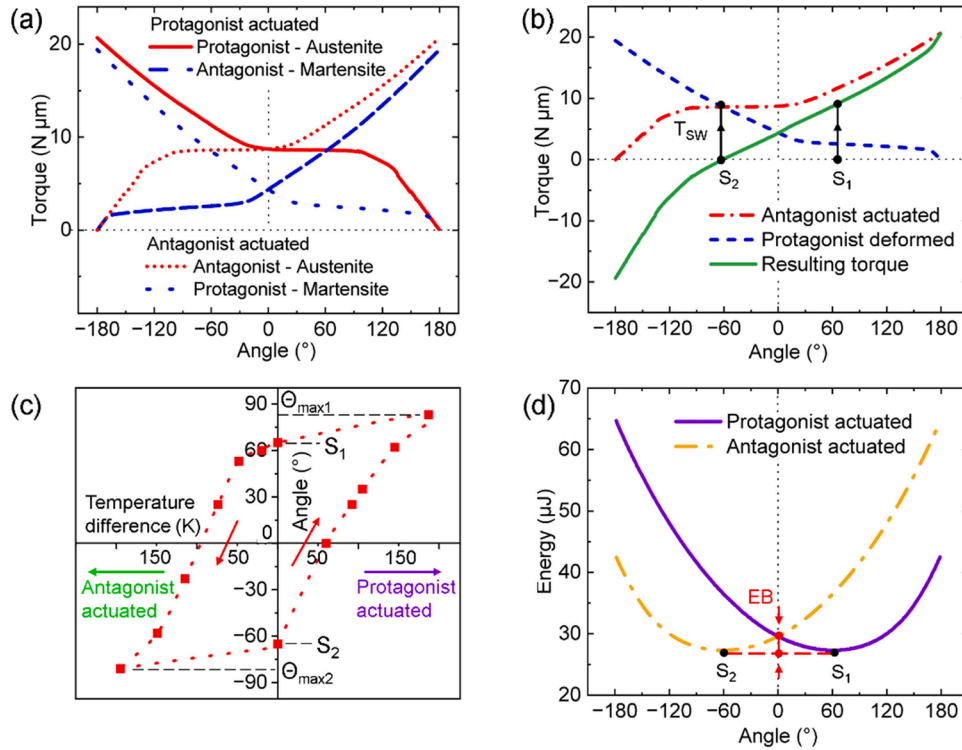


Fig. 7.2. Simulated mechanical performance of the bistable SMA folding microactuator with beam length L , width w , bending radius r , and thickness t being 2000 μm , 100 μm , 100 μm , and 20 μm , respectively. (a,b) Torque-angle characteristics of individual SMA double beams with opposing bending directions and of the corresponding coupled beam system. Either the protagonist or antagonist is heated above A_f , while the opposing double beam's temperature is below M_f . The switching torque T_{sw} is indicated. (c) Deflection versus temperature of the coupled beam system when selectively heating the protagonist and antagonist as indicated. The maximum angles $\Theta_{\text{max}1,2}$ and meta-stable positions $S_{1,2}$ are indicated. (d) Energy-angle characteristics of the coupled beam system when selectively heating the protagonist and antagonist. The energy barrier EB is indicated.

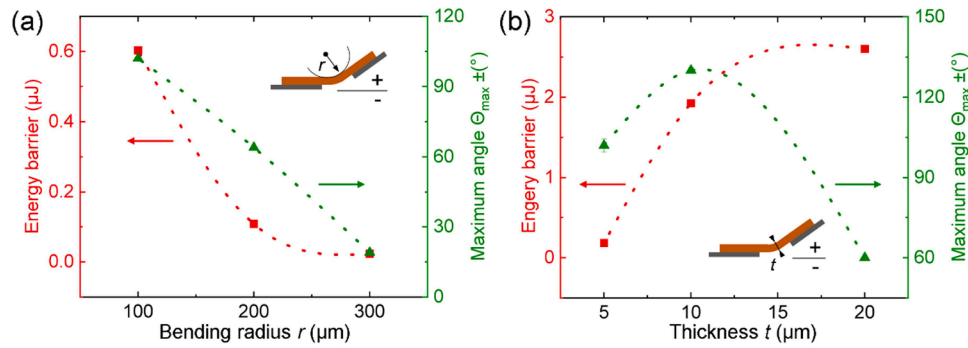


Fig. 7.3. Parametric simulation study to investigate the bistable response of the SMA folding microactuator at fixed beam length L of 2000 μm . (a) Energy barrier EB and maximum folding angle Θ_{\max} versus bending radius r at constant thickness t and width w of 5 μm and 300 μm , respectively. (b) Energy barrier EB and maximum folding angle Θ_{\max} versus thickness t at constant bending radius r and width w of 100 μm .

to induce the phase transformation to austenite. For a folding SMA actuator with dimensions of $2 \times 0.1 \times 0.02 \text{ mm}^3$, for instance, the time constants for switching between the end positions can be as low as 100 ms. However, the cooling rate required for reverse transformation limits the actuator's dynamics. This performance is governed by heat conduction and the forced heat convection self-induced by the folding motion. The frequency of reversible folding and unfolding is thus limited to about 1 Hz.

8. Trimorph PMMA/SMA/Si microactuator

The co-integration of silicon (Si) microstructures with micro-actuators has made significant advancements in various MEMS applications requiring active control, such as switching and tuning functions in mechanics and photonics applications. In particular, switching and tuning of optical signals in waveguide structures for next-generation communications systems demands for ultra-small scale actuators with high efficiency and large displacements [111]. Shape memory alloy (SMA) actuators meet those demands by offering high work density and scalability to nanometer dimensions. SMA actuators based on sputtered thin-film NiTiHf and NiTiCu in combination with Si technology have been demonstrated to produce large strokes in the order of several percent of actuator size [112,113]. The ultrasmall footprint of SMA/Si nanoactuator allows to combine with photonic components like waveguide structures in switching applications [114] and tunable waveguides as a key component in plasmonic modulators and plasmonic photodetectors [115]. By adding a third layer of polymer to such composites opens up the prospect of bistable actuation at the nanoscale [43, 116–118]. In the following, PMMA/SMA/Si trimorph microactuators are introduced and their functional properties are discussed with respect to their bistable behavior.

8.1. Geometry and layout

The trimorph microactuator design follows a beam cantilever layout, in which one end is fixed, and the other end is freely movable as shown in Fig. 8.1(a). It comprises three layers that are stacked on one another: a Si layer, a SMA layer of NiTiHf, and a PMMA layer. When subjected to a heat stimulus, the trimorph microactuator generates a bending moment based on stress states between three different layers resulting in two different stable states, as illustrated in Fig. 8.1(b). For direct Joule heating, a double-beam cantilever layout of these microactuators can be used as described in [118,119].

8.2. Actuation mechanism

The performance of the trimorph microactuator relies on the superimposing effects of differential thermal expansion, the shape memory effect, and differences in stiffness between the austenite and martensite phase [43]. For the bistability mechanism, we use a PMMA layer with glass transition temperature (T_g) that falls in between the martensite and austenite phase transformation temperatures (M_s and A_s) of the SMA as illustrated in Fig. 8.2(a). Assuming the trimorph microactuator is initially in stable state 2 (S_2), depicted in Fig. 8.2(b), switching to stable state 1 (S_1) requires the heating cycle up to T_2 , in which the microactuator is heated above the austenite finish temperature ($T_2 > A_f$). This enables the polymer to soften and conform to the deflected shape of the composite. Upon cooling below T_g and the martensite finish temperature M_f , the SMA layer transforms from austenite into unoriented martensite and the polymer hardens, thereby preserving the shape of state 1. To revert to stable state 2, the trimorph microactuator is heated to an intermediate temperature of T_1 ($T_g < T_1 < A_s$), causing the polymer to soften once more. Further cooling below M_f is associated with reorientation of martensite variants, which relaxes the

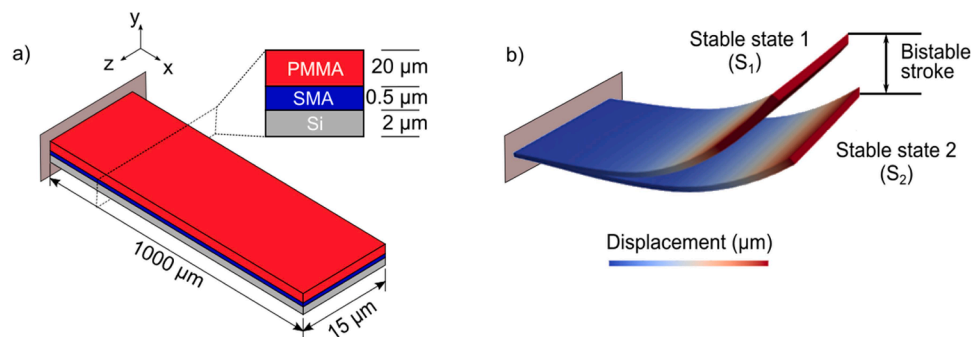


Fig. 8.1. Layout of a trimorph microactuator consisting of a PMMA/SMA/Si composite. (a) Beam cantilever with a length of 1000 μm , width of 15 μm and thicknesses of PMMA/SMA/Si layers of 20/0.5/2 μm . (b) Superimposed stable states 1 (S_1) and 2 (S_2) and resulting bistable stroke.

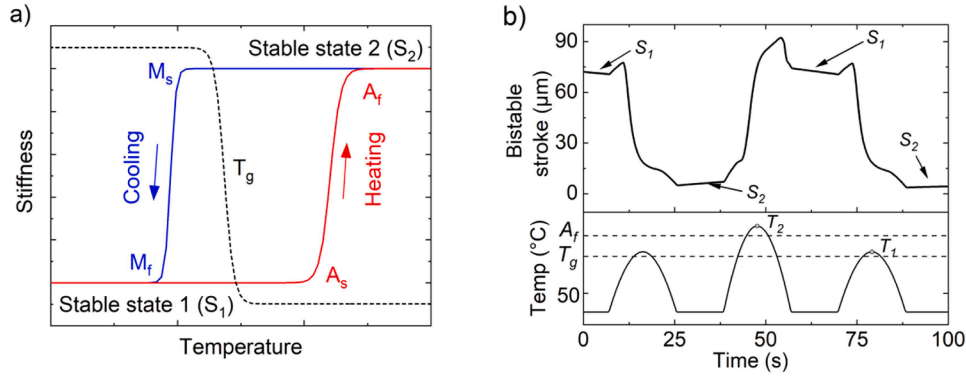


Fig. 8.2. (a) Schematic of interlaced polymer and SMA stiffness at different temperatures of a trimorph PMMA/SMA/Si microactuator. (b) Transient temperature cycles for bistable switching and its displacement characteristics of a trimorph microactuator with cantilever length of 1000 μm , width of 15 μm and PMMA/SMA/Si layer thicknesses of 20/0.5/2 μm .

internal stress and allows the microactuator to return to its initial shape.

Although various binary and ternary NiTi-based thin films have been explored for use in microactuators, TiNiHf SMAs are particularly suitable for this investigation due to their high transformation temperatures and large thermal hysteresis, which satisfies the conditions for bistability. In this study, transient simulations are conducted on a PMMA/TiNiHf/Si cantilever composite, starting from initial conditions of zero displacement and room temperature (20 $^{\circ}\text{C}$). Dirichlet boundary conditions are applied at the fixed end, and thermal eigenstrains are initially induced using established methods [42] to achieve stress-free conditions at the annealing temperature of 500 $^{\circ}\text{C}$. Joule heating is cyclically applied via a heat source acting on both the Si and TiNiHf layers of the beam cantilever. Heat convection on the top and bottom surfaces of the actuator is modeled using Robin-type boundary conditions, while convection on the remaining enclosed air surfaces is neglected [42,44].

8.3. Force and energy results

The bistability of the trimorph actuator is investigated by evaluating the energy barrier that is required to switch between two stable states. Fig. 8.3(a) illustrates the force-displacement behavior for the actuator with a cantilever length of 1000 μm , width of 15 μm , and PMMA/SMA/Si thicknesses of 20/0.5/2 μm . To switch from stable state 1 (S_1) to state 2 (S_2), the temperature is raised above the austenite finish temperature A_f , resulting in a combination of thermal expansion differences within the composite and phase transformation of the SMA. Below the glass transition temperature T_g and A_s , the composite remains stiff, exhibiting a typical bimorph effect and therefore a steep increase in force behavior. Once the temperature is above T_g , the PMMA layer softens, and as the

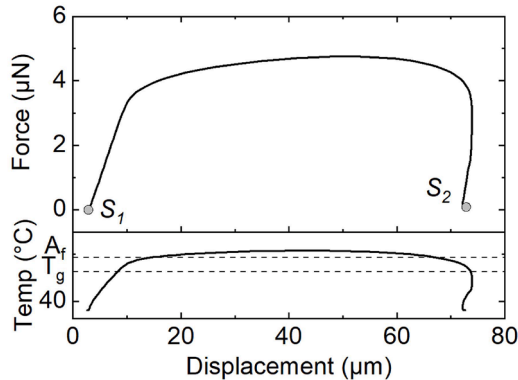


Fig. 8.3. Force-displacement curve of a trimorph PMMA/SMA/Si cantilever during heating-induced switching from stable state 1 (S_1) to stable state 2 (S_2).

temperature continues to rise, the displacement increases from 12 μm to 53 μm , where the maximum force is reached. Further heating results in a maximum displacement of about 72 μm . Upon cooling back to room temperature, the PMMA transitions to its rigid state below T_g , effectively locking the structure in the bent position at 72 μm . Thereby, the force drops to zero.

The trimorph microactuator exhibits a work output of approximately 0.25 nJ. To achieve this, the heat energy supplied must account not only for the phase transformation of the TiNiHf layer but also for the glass transition of the PMMA layer. For PMMA/SMA/Si thicknesses of 20/0.5/2 μm , the total thermal energy input required is estimated to be 2.4 μJ , resulting in an energy efficiency of about 0.01%. Therefore, the microactuator requires approximately 1.3 μW of input power to induce phase transformation within 1.8 s. The output power is around 0.05 nW, yielding a power efficiency of 0.005 %. The energy efficiency is lower compared to other actuation techniques. However, the bistable concept allows the microactuator to consume energy only when switching between its two stable states.

8.4. Bistability region

For bimorph SMA/Si actuators, the optimal thickness ratio has been studied and experimentally verified in previous work [118] to achieve a maximum deflection change. By adding the third layer PMMA to the device, there exists an optimal ratio of PMMA to SMA thicknesses to achieve a maximum bistable stroke, as shown in Fig. 8.4(a). If the polymer layer is too thin, it cannot hold the large deflections resulting from the SMA phase transformation. In contrast, if the PMMA layer is too thick, the composite becomes too stiff, leading to reduced bistable strokes. For a SMA layer thickness of 0.5 μm , a maximum bistable stroke of about 62 μm is achieved at a PMMA layer thickness of 20 μm .

The energy barrier is estimated by considering the work required to transition the trimorph cantilever beam between the stable states using Bernoulli's beam theory under elastic and plane strain conditions. The results obtained for different SMA and PMMA thicknesses are summarized in Fig. 8.4(b). The maximum of the energy barrier occurs between 20 and 25 μm , while the stroke maximum shifts to larger PMMA thicknesses for increasing SMA thickness. In particular, for a large SMA thickness of 2 μm , the stroke maximum is reached at about 40 μm . For ease of fabrication, the PMMA thickness should be as small as possible. A maximum stroke is achieved, e.g., for the layer thicknesses of SMA and PMMA of 0.5 μm and 20 μm , respectively. In this case, the energy barrier is about 72 pJ.

8.5. Dynamic actuator performance

The dynamic performance of the trimorph PMMA/SMA/Si

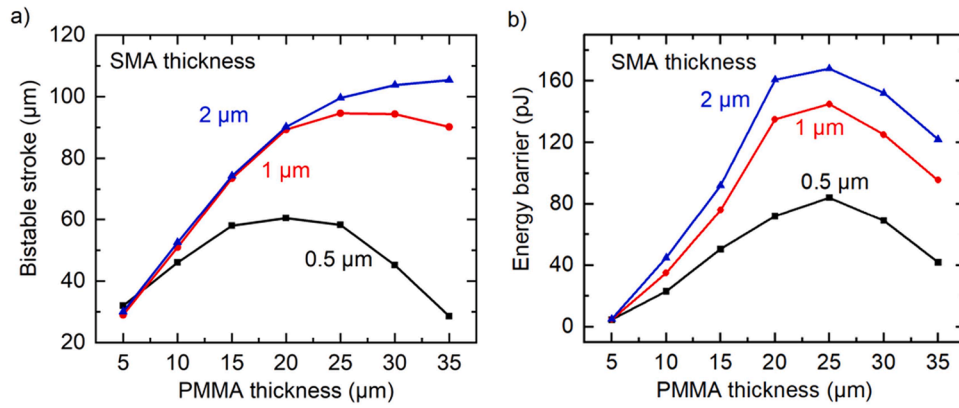


Fig. 8.4. Parametric study of SMA and PMMA layer thicknesses of the trimorph PMMA/SMA/Si microactuator. (a) Bistable stroke; (b) energy barrier required for switching between the stable states.

microactuator is governed by the heating and cooling rates achievable within a single actuation cycle. The simulated actuation cycle takes about 1.8 and 3.2 s of heating and cooling time, respectively. Thus, the operation frequency is approximately 0.2 Hz. The low frequency is due to the low thermal conductivity of the PMMA layer, making heat transfer inefficient. The PMMA layer must undergo a glass transition for switching between stable states, which reduces the actuation speed. Additionally, the PMMA layer dissipates heat much more slowly than the SMA layer, leading to prolonged cooling times.

9. Droplet-based multistable microactuator

Droplet-based microactuators are of special interest as they allow to realize almost “unlimited” throw. The droplets are moved by liquid dielectrophoresis. This effect is often mistakenly called electrowetting on dielectrics (EWOD), but originally, EWOD requires an electrical contact to the conductive liquid, while dielectrophoresis keeps the fluid completely isolated. The liquid can be either conductive or exhibit a high dielectric constant such as polar liquids (water, glycerol carbonate and others, see e.g. [120]). Inherently, a dense but thin isolation layer between the actuating electrodes and a hydrophobic coating is required, see e.g. [121] while a hydrophilic surface allows polar liquids to stick to the surface (permanent wetting). This can be used to move a platform on liquid bearings, see Fig. 9.1, [45,122]. The droplets are fixed by a small gap in the hydrophobic coating on the hydrophilic chip surface (Fig. 9.1 (a)). In this setting, a glider made of a e.g. silicon platform situated on those liquid bearings [123] can be actuated by electric forces. The complete simulation requires a complex model as this actuation principle is somewhere between open “digital microfluidics” as droplets are moved on a plain electrode field, and segmented flow, as the fluid is

moved in a channel-like structure between glider and electrode array. The gap between glider and the electrodes is defined by the interaction of the weight of the glider and the surface tension of the liquid as well as electrostatic forces [124]. To cover the overall dynamics of a droplet movement, a lumped parameter model as proposed in [125] can be utilized. An overview of fundamentals on actuate liquids can be found in [126].

Further applications of droplet-based multistable microactuators include microfluidic circuits and the manipulation and storage of biological substances, particularly for future medical diagnostics and lab-on-a-chip systems [127–129]. Future applications also include freely moving platforms as shown in Fig. 9.1, but on large planar electrode arrays for transportation or reconfiguration. In this case, the droplets act as roller bearings that are self-actuated.

9.1. Geometry and layout

Generally, liquids tend to form droplets with a minimal surface (spheres). Any deformation from this energy-minimal state requires external forces, e.g. gravitational force (own weight and external load from glider) or electrostatic forces [130]. The relationship of the different effects can be estimated by dimensionless characteristic numbers [131]. The gravitational force in relation to the surface tension is given by the Bond number: as long as the Bond number Bo (with $\Delta\rho$ the difference of the densities, the surface tension of the liquid, g the gravitational constant and R the radius of the droplet) is small $Bo \ll 1$, the liquid forms an almost perfect spherical droplet.

$$Bo = \frac{\Delta\rho}{\gamma} g R^2 \quad (9.1)$$

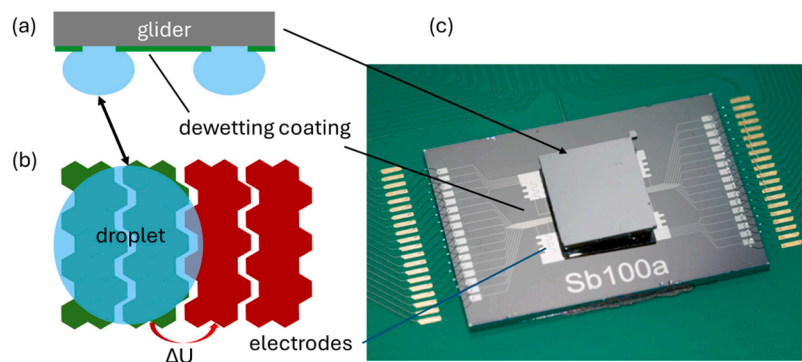


Fig. 9.1. (a) Schematic of a glider (grey) with two droplets (blue) fixed at local hydrophilic patterns within the hydrophobic coating (green); (b) electrode array; (c) realized glider with droplets on electrode array.

For Bond numbers $Bo > 1$, the droplet deforms under its own weight. Bo gives an estimation for the upper limit of the droplet size. For $Bo \cong 1$, a careful investigation must be performed as deformation and retracting surface tension are in the same order of magnitude. The external weight of the glider can be considered by an additional term in the Bond number:

$$Bo_{\text{(glider)}} = \frac{\Delta\rho}{\gamma} g R^2 + \frac{m_{\text{gl}}}{\gamma R} g \quad (9.2)$$

with m_{gl} : mass of the glider (for a glider with droplets $\frac{1}{4}$ of the total mass).

On the other hand, electrostatic forces influence the shape of a droplet: derived from the Bond number, a similar characteristic number is defined for the interaction of electrostatic forces and surface tension, the “electric Bond number” BO_e depending on the dielectric constants $\epsilon_0 \epsilon_r$ and the absolute value of the electrical field E .

$$BO_e = \frac{\epsilon_0 \epsilon_r}{\gamma} |E|^2 R \quad (9.3)$$

Here, the electrostatic force must exceed the retracting surface tension. Within a homogenous electrostatic field, the droplet is expanded in the direction of the electrodes for $BO_e > 1$.

For small Bond numbers Bo , the weight can be neglected and the droplet is mobile in all three normal directions. As suitable liquids exhibit reasonable dielectric constants (for water $\epsilon_r \approx 80$), the liquid is pulled into an electrical field; the most stable state is achieved when the liquid is situated within the area of highest field strength.

For droplet-based microactuators, the liquid should have a low vapor pressure and a high permittivity. A suitable long-term stable liquid is *glycerol carbonate*, a non-toxic, non-flammable, polar and non-volatile organic fluid with a melting point of -69°C and a permittivity around 80. Compared to water, it has a slightly lower surface tension ($57 \cdot 10^{-3} \text{ N/m}$ vs $73 \cdot 10^{-3} \text{ N/m}$ for water). As depicted in Fig. 9.2, water and glycerol carbonate have similar bond numbers Bo and BO_e . For droplets below 1 mm, both liquids exhibit Bond numbers well below 1. It should be mentioned, that BO_e scales with the applied electrical field; the printed curve represents a comparably low electrical field of 10 V/mm.

Due to the required hydrophobicity of the contact area, the droplet follows gravitational forces and drips down from an inclined surface as soon as the retracting electrostatic force is smaller than the gravitational force. A permanently multistable system needs additional barriers such as pillars on the surface. If the gap d between the pillars is smaller than the diameter of the droplet, it cannot pass through the gap: the retracting surface tension inhibits this. If an additional electrostatic force is applied, the droplet can squeeze through, as the electrostatic force increases the internal pressure of the liquid at the tip since the

pressure correlates to the radius of the droplet. This can be calculated by the Laplace pressure which describes the internal pressure in a droplet:

$$\delta p = p_{\text{in}} - p_{\text{out}} = 2 \frac{\gamma}{R} = \gamma \frac{dA}{dV} \quad (9.4)$$

For a deformed droplet, this pressure is given by

$$\delta p = p_{\text{in}} - p_{\text{out}} = \gamma \left(\frac{1}{R_1} + \frac{1}{R_2} \right). \quad (9.5)$$

It is obvious, that the smaller radius (here R_1) dominates and increases the pressure compared to a perfect, undeformed sphere. Pinning at the edge appears as long as the contact angle Θ_c is not exceeded by the angle resulting from the Laplace pressure at the gap d , $\Theta < \Theta_c$. For a completely dewetting surface, the critical Radius R is given by $R_1 \leq d/2$.

The required pressure is given by $p_{\text{in}} - p_{\text{out}} \gg \gamma \left(\frac{2}{d} \right)$ for a large droplet ($R \gg d$). For a droplet only slightly larger than the gap d ($2R \approx d$), the required pressure becomes $p_{\text{in}} - p_{\text{out}} \approx \gamma \left(\frac{4}{d} \right)$. A rough estimation of the electrical field strength $|E|^2$ for this limit case results from

$$BO_e = \frac{\epsilon_0 \epsilon_r}{\gamma} |E|^2 R > 1 \quad (9.6)$$

for a gap d with a width of approximately $2R$ of the droplet.

$$|E|^2 > \frac{\gamma}{\epsilon_0 \epsilon_r} \frac{2}{d} \quad (9.7)$$

The estimated local field strength of glycerol carbonate (GC) and water is depicted in Fig. 9.3 for droplets with a radius R between 20 μm and 1 mm and a gap width of approximately $2R$. When the gap and/or droplet size decreased the internal pressure increases, and the strength of the applied electrical field must be raised accordingly.

9.2. Actuation mechanism

The capacitance and thus the stored energy can be increased by increasing the dielectric constant within the capacitor: fluids move into the capacitor as their dielectric constant is higher than that of air, an effect frequently used to propel droplets. Here, droplets are connected to a movable platform (glider) in a hydrophilic area. They are restrained to a small, non-hydrophobic area while the remaining parts of platform and raceway are hydrophobic. Therefore, the droplets are both the moving part of the actuator and the bearing for the platform simultaneously.

Multistable actuation is achieved using alternating pairs of electrodes. While one pair of electrodes is switched off, the next one is addressed. This forces the fluid to move into the next semi-stable posi-

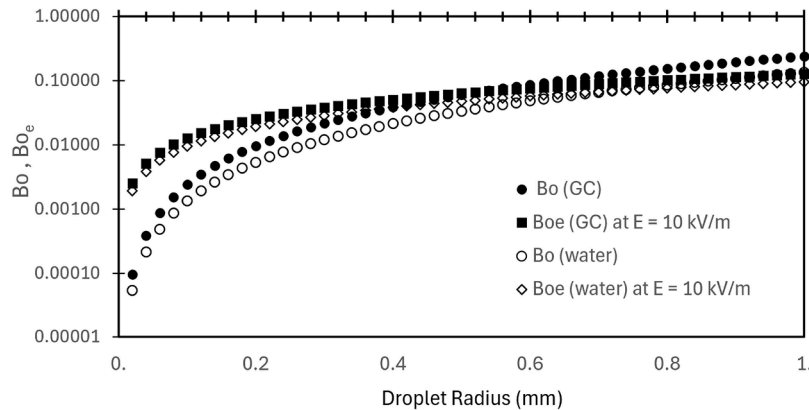


Fig. 9.2. Bond number and electrical Bond number versus droplet radius (between 20 μm and 1 mm) for glycerol carbonate (GC) and water; BO_e assumes an electrical field strength of 10 V / mm and scales with increasing voltage.

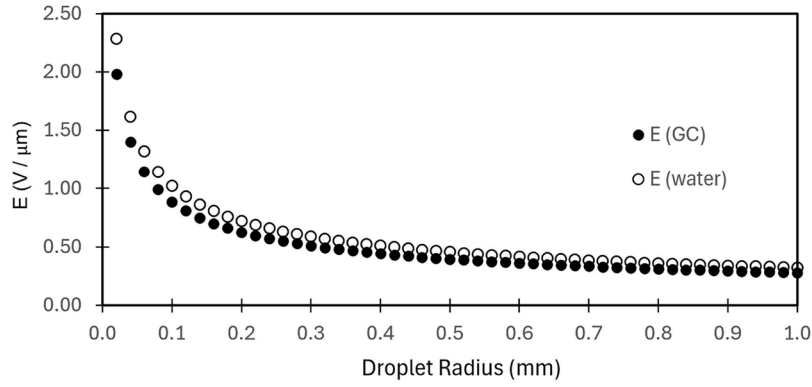


Fig. 9.3. Estimated local field strength for glycerol carbonate (GC) and water for droplets with a radius R between 20 μm and 1 mm and a gap width of approx. $2R$.

tion. The number of semi-stable states is given by the number of electrode pairs. For example, Fig. 9.4 is computed for a system with six electrodes and therefore three electrode pairs and three stable states. The stable stroke depicted in Fig. 9.4 is given by the length of the used electrodes, while the height of the energy barrier is determined by the capacitance change ΔC_E which is related to the droplet size and the electrode geometry (about 0.5 mm wide, with a droplet of about 1 mm). This state is stable as long as the dedicated electrodes are switched on. Therefore, this is a semi-stable condition.

As the capacitance C_E of a pair of electrodes depends on the position of the droplet, the electrostatic energy of the system also changes with the droplet position. To determine the capacity dependency of the system, finite element simulation can be performed for different positions. As an alternative, measurement data for an existing electrode can be used to train a neural network to approximate the capacitance. Using the formula for the stored energy E in a capacitor C_E : $E = 0.5 C_E V^2$, the energy of the system can be calculated for a given actuation voltage V , harnessing the neural network to compute the capacitance C_E . As an actuated system is stable at the position with the minimum negative energy, Fig. 9.4 shows the energy results for an electrode design with trapezoidal intersection area and the resulting energy barriers for the stable positions. By differentiating the electrostatic energy, the force displacement characteristic depicted in Fig. 9.4 can be computed.

If the electrodes of a tilted array are switched off, the glider moves following gravitational forces on the dewetting layer as the energy barrier caused by the electrical field is now missing. By introducing additional barriers (pillars) forming chambers around the electrodes, this effect can be effectively suppressed. When situated between a set of pillars, the droplet bending radius relaxes and the droplet reshapes into a sphere. In contrast, the intermediate situation with a bone-shape droplet is unstable: the droplet will follow any asymmetry and retract into one of the chambers. Therefore, it can be concluded that the diameter of each drop should contact at least two electrodes, see Fig. 9.5.

To initiate the movement, the next electrode can be activated (Fig. 9.5 (c)).

The two characteristic numbers Bo and Bo_e allow to estimate the behavior of the system and to determine some principal requirements for the layout. With respect to a permanent multistability, pillars are a suitable way to counteract “gravitational effects” that occur from the required hydrophobic coatings. Pillars with surface angles below the local contact angle of the droplet successfully prevent it from moving. This effect is well-known from applications in “digital microfluidics”, e. g. in electronic paper, but has also been used for optical switches [132].

The additional pressure p_{es} caused by electrostatic forces is required to achieve a surface angle exceeding the contact angle. This enables the droplet to pass through the gap between the pillars. Main geometrical

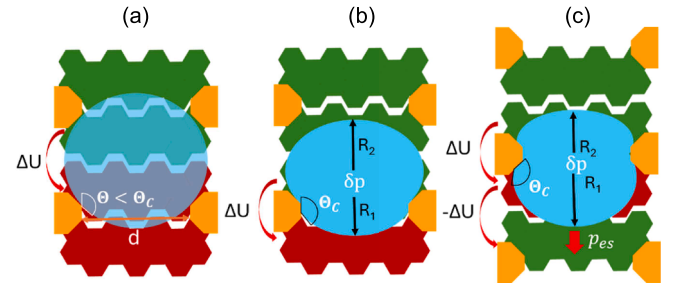


Fig. 9.5. Schematic of multistable droplet actuation. (a) Stable position of the droplet in between pillars (orange). The droplet is held by the applied voltage between the electrodes shown in red and green color. The surface angle is smaller than the contact angle. (b) Start of movement through the gap by the applied voltage between the electrodes shown in red and green color. The surface angle approaches the contact angle of liquid and surface. (c) A second potential difference ΔU is applied to increase the electrostatic pressure p_{es} that pushes the droplet into the next stable position by reducing the radius R_1 .

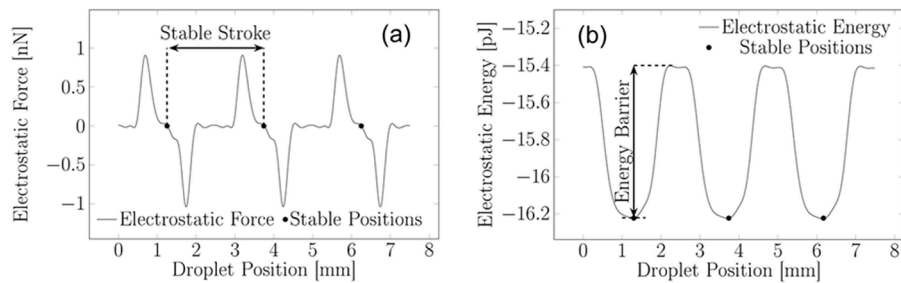


Fig. 9.4. Force-displacement (a) and energy-displacement (b) results for a droplet-based microactuator with three electrode pairs (for metastable actuation, without pillars). The electrode width is assumed to be 0.5 mm at an actuation voltage 1 V. The waved gap between the electrodes is a few μm .

parameters are the ratio between the gap and the diameter of the droplet as well as the angle of the pillars. As soon as the ratio nears ≥ 1 (droplet size larger than the gap), the required voltage is minimized. The angle at the pillars in combination with the sphere radius defines the required pressure difference and thus allows to adjust the switching voltage with respect to geometrical as well as fluid parameters. For a detailed and more precise simulation of the required voltages in a 3D system with spherical droplets, a numerical simulation is required, but the given simple assumptions fully describe the principle of operation. The electrostatic force scales with $1/R$: smaller droplets and/or gaps require higher electrostatic fields while the upper limit is given by $Bo \approx 1$.

In a comparable system, the force of the droplet actuators was calculated by FEM simulations to be $9.85 \mu\text{N}$ over a distance of $500 \mu\text{m}$ taking into account air resistance and the interface between the droplet and the chip [122]. It should be noted, that the formation of a droplet and its deformation are comparable to a mechanical spring. Therefore, most of the spent electrical energy is stored within the droplet and released after switching off. The corresponding mechanical work was about 4.9 nJ . In this case, the electrical energy supplied to the system was about 6.3 nJ considering the applied voltage of 42 V and a capacitance in the range $5.5 - 7.2 \text{ pF}$ [125]. The corresponding energy efficiency is estimated to be as high as 78% , which can be attributed to the low energy losses due to heat, friction, and viscosity compared to other microactuator principles [133]. Here, it should also be noted, that significant parts of the capacitance are caused within the electrodes (electrode on isolated substrate).

9.3. Multistability region

For droplet-based systems, there are two types of multistability: On a plain electrode array, the droplet is stable on two neighboring electrodes with a potential difference (see Figs. 9.1, 9.4) as long as a voltage is applied. Without voltage, the sphere may displace due to gravitational forces as soon as the electrode array is even slightly tilted. A true multistable region is achieved by introducing “pillars” as shown in Fig. 9.5. The droplet will stay inside the cavity within in the restraining pillars as long as the diameter of the drop is larger than the gap between two pillars. During actuation a voltage is applied at electrodes across the pillars (Fig. 9.5 (b,c) and the electrostatic force on the droplet is able to overcome the barrier. The required energy level depends on the ratio of the droplet diameter vs. pillar gap width which should only be about 10% higher than 1 to overcome the restoring surface tension. Unlike intuitive expectations, smaller droplets generally require higher field strength than larger droplets. With diminishing droplet size the surface to volume ratio increases which results in increasing surface tension as well as a markedly raised effect of evaporation even from low-vapor pressure solvents like GC. A detailed calculation of energies for the multistable system is difficult as also the shape and the surface energy of all surfaces need to be considered.

9.4. Dynamic actuator performance

The main focus of this investigation is the steady-state performance of the droplet-based multistable microactuator based on EWOD. Owing to the small masses of the droplets, the time constants of the microactuators are small, typically in the range between 2 and 100 ms [125]. High droplet velocities of 6 mm/s are achieved over a distance of several mm [122]. Taking into account the droplet size, the viscosity and surface tensions of the liquid, electrode geometries, and mechanical overshoot of the droplet, the corresponding frequencies can reach several hundred Hz . It should be noted, that the spring constant of a droplet increases with decreasing droplet diameter (surface tension) while the mass decreases. Bond and electrical Bond number both decrease with scaling the droplet.

10. Results and discussion

This review addresses recent developments of active bi- and multistable microactuator systems. Active bi-/multistability means that no external force for switching between states is required. Instead, cooperative microactuators are used to actively control energy levels and, thus, to trigger force instabilities and corresponding switching events. This approach is of special interest at miniature scales as size constraints and energy minimization become critical. Generally, various actuation principles can be exploited to achieve this functionality. However, each principle involves specific transducer materials and system architectures, which impose constraints on fabrication and miniaturization. Furthermore, the close vicinity of transducer materials and functional structures causes various coupling effects that need to be understood. Therefore, it is important to assess the different approaches in terms of bi-/ multistable performance and to evaluate the effect of design parameters as well as specific limitations. Here, we present selected examples of bi-/multistable microactuator systems covering various principles including the shape memory effect, dielectric elastomer (DE) effect, magnetic and electrostatic principles as well as combinations thereof. Thereby, we assess the different concepts with respect to their energy characteristics and critical forces taking into account system dimensions.

The basic requirements for achieving bi- and multistability can be summarized as follows:

- Stable deflection states are characterized by energy minima that are separated by an energy barrier.
- The energy barrier should be high enough to stabilize the deflection states, but it should allow for switching between stable states.
- The corresponding latching force should be sufficiently low or it should be controllable that it can be overcome by the switching force. In this respect, the maximum switching force poses a limit to the latching force.
- The switching force must not change its sign in between stable states. Therefore, the minimum force of the force-displacement characteristics becomes a critical metric, which characterizes the reliability of switching with respect to external forces. Bi-/ multistability is lost if the switching force becomes zero in between the stable states.

Table 10.1 gives an overview on the performance metrics of the presented bi-/multistable microactuator systems. The overall dimensions of these demonstrators are in the mm range. Bi- and multistability are achieved by making use of instabilities caused by nonlinear force versus displacement characteristics. This performance is obtained, e.g., by compliant structures of smart materials like DE membranes (Section 3) and clamped SMA beams (Section 6). However, compliant structures require sufficiently high aspect ratios, which poses a challenge to their fabrication and limits their miniaturization to μm dimensions. Another option is using magnetic force instabilities that occur at large magnetic field gradients (Section 5), which can be generated by miniature permanent magnets or miniature coils. This concept is further extended in Section 4 to achieve magnetic levitation and to use the force instability of a superimposed electric field. Realization of these concepts is challenging as well, as large magnetic fields are difficult to realize at small scales and miniaturization is limited therefore. In this respect, the use of electrostatic actuation principles is attractive. As discussed in Section 9, electrostatic actuators can be scaled to micrometer dimensions due to precise fabrication of electrodes and droplet sizes can reach tens of μm . Another option is the use of material nonlinearities. SMA materials are well known to exhibit highly nonlinear stress-strain characteristics in martensitic state [104], which are exploited in Sections 6, 7 and 8. Applying a sufficiently large stress causes reorientation of martensite variants, which are metastable and, thus, gives rise to quasi-plastic deformation, which can be recovered on demand by heating to the austenite state. Therefore, SMA beam cantilevers adopt

Table 10.1

Overview on the performance metrics of the presented bi-/multistable microactuator systems. The critical switching force F_{sw} denotes either the maximum force of the force-displacement characteristics required to overcome a latching force or the minimum force of the force-displacement characteristics if a force minimum occurs in between the stable states. The direction dependencies of F_{sw} and energy barriers EB are indicated.

Sect.	Bi-/multistable mechanism	Dimensions (mm ³)	Design parameter (s)	Critical switching force F_{sw} (mN)	Energy barrier EB (μJ)
3	Coupling of antagonistic monostable DE beams with a bistable polymer beam	$50 \times 3 \times 5$	Beam length l , beam width b	+ direction: 970 ^{..} – direction [*] : 350 ^{..}	+ direction: 590 – direction: 2.850
4	Combined magnetic-electric force instability	$10 \times 10 \times 2$	Coil height h_c , Coil radius r_l	+ range: 0.001 – range: 0.008	+ range: 0.0007 – range: 0.0023
5	Multiple magnetic latching within a stack of thin ring-shaped ferro-magnetic plates [*]	$11.5 \times 11.5 \times 10.5$	vertical positions of steel rings z_1 and z_2	+ direction: $F_{sw1,2} = 1.3, 1.6$ – direction: $F_{sw1,2} = 5.2, 3.8$	+ direction: $EB_{1,2} = 1.8, 1.7$ – direction: $EB_{1,2} = 2.2, 1.3$
6	Antagonism of coupled monostable SMA beams	$10 \times 1 \times 2$	Spacer length S , Pre-deflection h	+ direction: 5.7 – direction: 5.7 ^{...}	+ direction: 5.600 – direction: 95.000
7	Antagonism of coupled SMA cantilevers	$10 \times 22 \times 0.14$	Beam thickness t , bending radius r	± direction: 8.7 ^{...}	± direction: 2.6
8	Fixation of shape memory bimorph deflection through polymer glass transition	$1 \times 0.015 \times 0.023$	PMMA layer thickness	+ direction: 0.0047	+ direction: $72 \cdot 10^{-6}$
9	Multiple electrostatic force instability (n – number of electrodes)	$1 \times 1 \times 2n$	Bond numbers BO and BO_{es} , droplet diameter vs. gap size	± direction: 10^{-6}	± direction: $8 \cdot 10^{-7}$

^{*} Tristable actuator system.

^{..} Minimum force of the non-linear force-displacement characteristics between the stable equilibrium positions.

^{...} Minimum switching force at 1.8 kV.

^{...} Torque in (mN·mm).

metastable deflection states (Section 7). As martensite variants may form at various length scales down to the nanometer scale, this mechanism has a particularly high miniaturization potential [112]. SMA bimorph cantilevers may require an additional latching mechanism to withstand the reset force of the substrate layer. This is achieved in Section 8 by making use of the glass transition of an additional PMMA layer.

Depending on the object (mass, size, geometry) under consideration for switching, the requirements on switching force and energy barrier may vary considerably as can be inferred from Table 10.1. The DE beam actuators need to be designed sufficiently large and a high voltage is required to generate a large enough switching force. In both cases, the antagonistic coupling of the beam actuators gives rise to an asymmetry of the energy landscape and, thus, direction-dependent switching forces. The DE beam actuators form a base unit for multistable switching arrays as shown in Fig. 10.1, which enable the development, e.g. of soft conveyors or conformable multi-unit tactile displays [52].

Compliant structures of smart materials like DE membranes (Section 3) or clamped SMA beams (Section 6) give rise to relatively large barrier heights and, thus, large stability with respect to external forces. The characteristics of switching force F_{sw} and energy show a highly nonlinear course in between the stable states. In particular, a force minimum occurs at intermediate positions between the stable states, which is considered to be the critical switching force that must not become zero to enable bistability. The critical switching forces are in the mN range. The clamped SMA beams need to be designed with a sufficiently large pre-strain to achieve active bistability, which can be adjusted by the spacer length S and pre-deformation h .

The antagonism of coupled SMA cantilevers in the origami-inspired microactuator system (Section 7) is characterized by a barrier height of a few μJ. Due to the antagonistic coupling of the beam actuators the performance also depends on the switching direction. Depending on the mass of the tiles, the low barrier height may not provide for sufficient stability against external forces. Therefore, an additional latching mechanism may be required. One option is the integration of additional magnetic microstructures to enable magnetic latching. By the integration of a soft-magnetic layer of NiMnGa with ferromagnetic transition at about 98 °C, the magnetic latching force can be controlled by Joule heating, which opens up the option of reversible latching and, thus, folding and unfolding on demand [106]. Here, the critical torque to overcome the latching torque is about 8.7 μNm in unheated metastable state. This torque is well exceeded by the switching torque generated

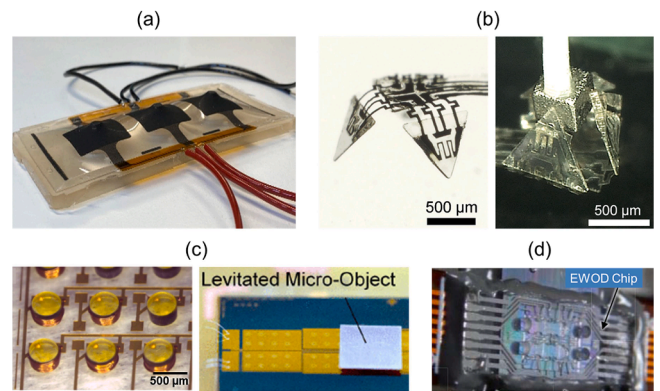


Fig. 10.1. Multistable microactuator systems based on the presented bistable microactuator concepts: (a) Multistable 1-by-3 DE microactuator array [52]; (b) multistable origami-inspired microactuator system consisting of four tiles interconnected by antagonistic SMA folding beams. The left / right photo shows the system with all tiles deflected downwards without / upwards with magnetic latching [106]; (c) distributed solenoid micro-coil system for multistable levitation and transportation [134,135]; (d) photograph of a droplet-based microoptical switch. The overall size of the fluidic chip is $4.5 \times 12 \text{ mm}^2$ [132].

upon selective heating the protagonist/antagonist beam to austenitic state. The presented system consisting of two tiles is the basic building block of multistable origami-inspired microactuator systems. One example is a microactuator system consisting of four tiles as shown in Fig. 10.1, in which each tile can switch between an upwards or downwards deflection state allowing for different metastable 3D shapes, e.g. a table or a pyramid [106]. Further miniaturization and parallelization to coupled multistable arrays of sub-micron tiles enables the development of re-programmable micromatter that can adapt various 3D shapes on demand.

The deposition of an additional polymer layer with a glass transition onto a bimorph SMA microactuator is an interesting approach to tune the energy barrier in a large range. As shown in Section 8, the PMMA layer in glassy state gives rise to an energy barrier of about 72 pJ, which is sufficient to maintain the deflection of the SMA bimorph. On the other hand, it is soft enough above the glass transition to enable the deformation of the SMA bimorph in austenitic state and the reset motion in martensitic state. Consequently, a low force of a few μN is sufficient for

switching between stable states. These results indicate that further miniaturization of this concept is an interesting approach to realize compact bistable microswitches [43].

The magnetic actuator system is characterized by barrier heights in the range of a few μJ and critical switching forces of a few mN (Section 5). Depending on the choice of design parameters, also intermediate positions are stabilized and, thus, tristable performance is possible. The built-in asymmetry of the actuator system causes a direction-dependent switching performance. By adding more ferromagnetic layers, the system may be further extended to multistable systems for digital positioning.

The lowest energy barriers are present in the electrostatic microactuator system (Section 8). Here, a barrier height in the order of pJ is sufficient to trap a droplet with a radius in the order of 500 μm . Consequently, the switching of their position requires forces only in the nN range. The energy barrier can be tuned by the ratio of droplet diameter and gap size in between pillars. The concept of droplet-based microactuation has been combined with silicon photonics to establish a non-volatile fiber optic switch as shown in Fig. 10.1, which enables new applications ranging from datacenters over core networks to access networks.

Similarly, barrier heights and switching forces are low in the case of magnetic levitation of small masses having a weight of a few μN (Section 5). Recently, distributed micro-coil systems have been developed to enable for multistable levitation and transportation of miniature objects [134,135].

In dynamic applications, the switching time and frequency are additional important metrics. Depending on the actuation principle, typical frequencies range from 1 Hz in case of SMA-based microactuation, about 25 Hz for millimeter-size magnetic lift actuation and 100 Hz in the case of DE actuation. Electrostatic and inductive levitation microactuators may reach 1 kHz and more. The energy efficiency of actuation between stable positions is in the order of 0.5% in the case of SMA-based microactuation and even less in the case of magnetic lift actuation. Electrostatic and droplet-based microactuators reach the highest efficiencies in the order of 70 and 80 %, respectively.

11. Conclusions

This review presents selected concepts of cooperative microactuator systems to generate active bi- and multistability requiring no external force for switching between stable states. Switching between stable states is achieved via selective control of the microactuators in order to tune energy levels and, thus, to trigger force instabilities and corresponding switching events. This approach is of special interest at miniature scales due to size and power constraints. The presented concepts comprise different transducer materials and system architectures covering electrostatic, magnetic, dielectric elastomer and SMA principles. At first, each concept is introduced and typical performance characteristics are presented. The influence of key design parameters on the bi-/multistable performance characteristics is discussed. In many cases, asymmetries caused by the design or fabrication result in a direction dependence of the bistable performance. Depending on the object (mass, size, geometry) under consideration for switching, the energy landscapes and corresponding energy barriers vary considerably from pJ (droplet microactuator systems and magnetic levitation) to mJ (SMA and DE actuator systems). Consequently, the switching forces cover the range from nN to mN, respectively.

The presented results reflect the breadth of new concepts that have been developed in recent years. These concepts enable digital mechanical positioning of various objects with a wide range of switching forces. Current research pursues two major trends. One trend is in further miniaturization from mm dimensions down to the μm range. Among the presented concepts, electrostatic and shape memory microactuator systems have a particularly high downscaling potential as can be inferred from the fundamental scaling laws of electrostatic and shape

recovery forces, as the force density increases for decreasing size according to $F/V \sim r^{-1}$ [104]. Furthermore, the deposition and micro-machining of metal and SMA films is well established in MEMS technology allowing to fabricate micro and nano-scale structures thereof. The second trend is the increase of functionality through parallelization of bistable microactuator systems in one or two directions, which leads to advanced multistable microactuator arrays. This will open up new options in the emerging fields of digital micromechanical systems, digital microoptics and digital microfluidics as well as reprogrammable micromatter that can adapt its 3D shape on demand.

CRedit authorship contribution statement

Manfred Kohl: Writing – review & editing, Supervision, Resources, Project administration, Methodology, Funding acquisition, Conceptualization. **Christoph Ament:** Supervision, Resources, Project administration, Methodology, Funding acquisition, Conceptualization. **Gowtham Arivanandhan:** Writing – original draft, Visualization, Validation, Investigation, Formal analysis, Data curation. **Tamara Bechtold:** Supervision, Software, Project administration, Methodology, Funding acquisition, Conceptualization. **Peter Conrad:** Writing – original draft, Visualization, Validation, Software, Investigation, Formal analysis, Data curation. **Sipontina Croce:** Visualization, Validation, Investigation, Formal analysis, Data curation. **Vincent Gottwald:** Writing – original draft, Visualization, Validation, Software, Methodology, Investigation, Formal analysis, Data curation. **Martin Hoffmann:** Writing – original draft, Supervision, Resources, Project administration, Methodology, Funding acquisition, Conceptualization. **Jonas Hubertus:** Visualization, Validation, Methodology, Investigation, Formal analysis, Data curation. **Alexander Kopp:** Writing – original draft, Visualization, Validation, Software, Methodology, Investigation, Formal analysis, Data curation. **Zixiong Li:** Visualization, Validation, Methodology, Investigation, Formal analysis, Data curation. **Michael Olbrich:** Writing – original draft, Visualization, Validation, Software, Methodology, Investigation, Formal analysis, Data curation. **Kirill Poletkin:** Writing – original draft, Visualization, Validation, Supervision, Software, Project administration, Methodology, Investigation, Funding acquisition, Formal analysis, Conceptualization. **Alberto Priuli:** Writing – original draft, Visualization, Validation, Investigation, Formal analysis, Data curation. **Gianluca Rizzello:** Writing – original draft, Validation, Supervision, Project administration, Funding acquisition, Conceptualization. **Arwed Schuetz:** Writing – original draft, Visualization, Validation, Software, Methodology, Investigation, Formal analysis, Data curation. **Guenter Schultes:** Supervision, Project administration, Methodology, Funding acquisition, Conceptualization. **Stefan Seelecke:** Supervision, Resources, Project administration, Funding acquisition, Conceptualization. **Lena Seigner:** Visualization, Validation, Software, Methodology, Investigation, Formal analysis, Data curation. **Hamid Shahsavari:** Writing – original draft, Visualization, Validation, Software, Methodology, Investigation, Formal analysis. **Muhammad B. Shamim:** Visualization, Validation, Software, Formal analysis, Data curation. **Marian Sielenkämper:** Visualization, Validation, Software, Methodology, Investigation, Formal analysis, Data curation. **Georgino K. Tshikwand:** Writing – original draft, Visualization, Validation, Software, Investigation, Formal analysis, Data curation. **Ulrike Wallrabe:** Writing – review & editing, Validation, Supervision, Resources, Project administration, Methodology, Funding acquisition, Conceptualization. **Pascal Weber:** Visualization, Validation, Investigation, Formal analysis, Data curation. **Frank Wendler:** Validation, Supervision, Resources, Project administration, Funding acquisition. **Stephan Wulfinghoff:** Validation, Supervision, Resources, Project administration, Conceptualization.

Declaration of competing interest

The authors declare that they have no known competing financial

interests or personal relationships that could have appeared to influence the work reported in this paper.

Acknowledgements

This work was funded by the German Research Foundation (Deutsche Forschungs-gemeinschaft, DFG) through the priority program “Cooperative Multistage Multistable Microactuator Systems” (SPP2206).

Data availability

Data will be made available on request.

References

- [1] J. Castillo-León, W.E. Svendsen, Lab-on-a-Chip Devices and Micro-Total Analysis Systems, Springer, Berlin, 2015, <https://doi.org/10.1007/978-3-319-08687-3>.
- [2] A. Manz, J.S. O'Connor, P. Neuzil, G. Simone, Microfluidics and Lab-On-A-Chip, R. Soc. Chem. (2020), <https://doi.org/10.1039/9781839169236>.
- [3] Ai-Q Liu, RF MEMS Switches and Integrated Switching Circuits, Springer, Berlin, 2010, <https://doi.org/10.1007/978-0-387-46262-2>. ISBN 0387462619.
- [4] Yu-X Ren, R-De Lu, L. Gong, Tailoring light with a digital micromirror device, Ann. Phys. 527 (7–8) (2015) 447–470, <https://doi.org/10.1002/andp.201500111>.
- [5] A.S. Algarni, M.H.M. Khir, J.O. Dennis, et al., A review of actuation and sensing mechanisms in MEMS-based sensor devices, Nanoscale Res. Lett. 16 (2021) 16, <https://doi.org/10.1186/s11671-021-03481-7>.
- [6] G. Pillai, S.S. Li, Piezoelectric MEMS resonators: a review, IEEE Sens. J. 21 (11) (2021) 12589–12605, <https://doi.org/10.1109/JSEN.2020.3039052>.
- [7] I. Stachiv, E. Alarcon, M. Lamac, Shape memory alloys and polymers for MEMS/NEMS applications: review on recent findings and challenges in design, preparation, and characterization, Metals 11 (2021) 415, <https://doi.org/10.3390/met11030415>.
- [8] M. Kohl, S. Seelecke, U. Wallrabe, Cooperative Microactuator Systems (Eds.), MDPI, Basel, Switzerland, 2023, <https://doi.org/10.3390/books978-3-0365-8235-1>.
- [9] M. Kohl, S. Seelecke, S. Wulfinhoff, Cooperative Microactuator Devices and Systems, MDPI, Basel, Switzerland, 2024, <https://doi.org/10.3390/books978-3-7258-0901-1>.
- [10] Y. Cao, M. Derakhshani, Y. Fang, G. Huang, C. Cao, Bistable structures for advanced functional systems, Adv. Funct. Mater. 31 (2021) 2106231, <https://doi.org/10.1002/adfm.202106231>.
- [11] Y. Chi, Y. Li, Y. Zhao, Y. Hong, Y. Tang, J. Yin, Bistable and multistable actuators for soft robots: structures, materials, and functionalities, Adv. Mater. 34 (2022) 2110384, <https://doi.org/10.1002/adma.202110384>.
- [12] B.D. Jensen, M.B. Parkinson, K. Kurabayashi, L.L. Howell, M.S. Baker, Design optimization of a fully-compliant bistable micro-mechanism, in: Proceedings of the ASME International Mechanical Engineering Congress and Exposition 35555, American Society of Mechanical Engineers, 2001, pp. 357–363, <https://doi.org/10.1115/IMECE2001/MEMS-23852>.
- [13] J. Tsay, L.Q. Su, C.K. Sung, Design of a linear micro-feeding system featuring bistable mechanisms, J. Micromech. Microeng. 15 (2005) 63–70, <https://doi.org/10.1088/0960-1317/15/1/010>.
- [14] C. Goll, W. Bacher, B. Buestgens, D. Maas, W. Menz, W.K. Schomburg, Microvalves with bistable buckled polymer diaphragms, J. Micromech. Microeng. 6 (1) (1996) 77–79, <https://doi.org/10.1088/0960-1317/6/1/017>.
- [15] M. Dorfmeister, M. Schneider, U. Schmid, Static and dynamic performance of bistable MEMS membranes, Sens. Actuators A Phys. 282 (2018) 259–268, <https://doi.org/10.1016/j.sna.2018.09.038>.
- [16] T. Huesgen, G. Lenk, T. Lemke, P. Woias, Bistable silicon microvalve with thermoelectrically driven thermopneumatic actuator for liquid flow control, in: Proceedings of the IEEE 23rd International Conference on Micro Electro Mechanical Systems (MEMS), 2010, pp. 1159–1162, <https://doi.org/10.1109/MEMS.2010.5442417>.
- [17] Y. Zhang, G. Ding, S. Fu, B. Cai, A fast switching bistable electromagnet microactuator fabricated by UV-LIGA technology, Mechatronics 17 (2–3) (2007) 165–171, <https://doi.org/10.1016/j.mechatronics.2006.06.003>.
- [18] J. Barth, B. Krevet, M. Kohl, A bistable SMA microactuator with large work output, in: Proceedings of the TRANSDUCERS 2009 International Solid-State Sensors, Actuators and Microsystems Conference, IEEE, 2009, pp. 41–44, <https://doi.org/10.1109/SENSOR.2009.5285568>.
- [19] J. Barth, B. Krevet, M. Kohl, A bistable shape memory microswitch with high energy density, Smart Mater. Struct. 19 (9) (2010) 094004, <https://doi.org/10.1088/0964-1726/19/9/094004>.
- [20] J. Barth, C. Megnin, M. Kohl, A bistable shape memory alloy microvalve with magnetostatic latches, J. Microelectromech. Syst. 21 (1) (2011) 76–84, <https://doi.org/10.1109/JMEMS.2011.2174428>.
- [21] W. Hamouche, C. Maurini, S. Vidoli, A. Vincenti, Multi-parameter actuation of a neutrally stable shell: a flexible gear-less motor, Proc. R. Soc. A Math. Phys. Eng. Sci. 473 (2017) 20170364, <https://doi.org/10.1098/rspa.2017.0364>.
- [22] H. Shao, S. Wei, X. Jiang, D.P. Holmes, T.K. Ghosh, Bioinspired electrically activated soft bistable actuators, Adv. Funct. Mater. 28 (2018) 1802999, <https://doi.org/10.1002/adfm.201802999>.
- [23] E.G. Loukaides, S.K. Smoukov, K.A. Seffen, Magnetic actuation and transition shapes of a bistable spherical cap, Int. J. Smart Nano Mater. 5 (2014) 270–282, <https://doi.org/10.1080/19475411.2014.997322>.
- [24] X. Hou, Y. Liu, G. Wan, Z. Xu, C. Wen, H. Yu, J.X.J. Zhang, J. Li, Z. Chen, Magneto-sensitive bistable soft actuators: experiments, simulations, and applications, Appl. Phys. Lett. 113 (2018) 221902, <https://doi.org/10.1063/1.5062490>.
- [25] H. Hussein, F. Khan, M.I. Younis, A monolithic tunable symmetric bistable mechanism, Smart Mater. Struct. 29 (2020) 075033, <https://doi.org/10.1088/1361-665X/ab8ea3>.
- [26] T. Chen, K. Shea, An autonomous programmable actuator and shape reconfigurable structures using bistability and shape memory polymers, 3D Print. Addit. Manuf. 5 (2018) 91–101, <https://doi.org/10.1089/3dp.2017.0118>.
- [27] H.Y. Jeong, E. Lee, S. Ha, N. Kim, Y.C. Jun, Multistable thermal actuators via multimaterial 4D printing, Adv. Mater. Technol. 4 (2019) 1800495, <https://doi.org/10.1002/admt.201800495>.
- [28] A.F. Arrieta, V. Van Gemmeren, A.J. Anderson, P.M. Weaver, Dynamics and control of twisting bistable structures, Smart Mater. Struct. 27 (2018) 025006, <https://doi.org/10.1088/1361-665X/aa96d3>.
- [29] P.F. Giddings, H.A. Kim, A.I.T. Salo, C.R. Bowen, Modelling of piezoelectrically actuated bistable composites, Mater. Lett. 65 (2011) 1261–1263, <https://doi.org/10.1016/j.matlet.2011.01.015>.
- [30] X. Chen, L. Bumke, E. Quandt, M. Kohl, Bistable actuation based on antagonistic buckling SMA beams, Actuators 12 (2023) 422, <https://doi.org/10.3390/act12110422>.
- [31] S. Hau, G. Rizzello, M. Hodgins, A. York, S. Seelecke, Design and control of a high-speed positioning system based on dielectric elastomer membrane actuators, IEEE/ASME Trans. Mechatron. 22 (3) (2017) 1259–1267, <https://doi.org/10.1109/TMECH.2017.2681839>.
- [32] S. Croce, J. Neu, J. Hubertus, S. Seelecke, G. Schultes, G. Rizzello, Model-based design optimization of soft polymeric domes used as nonlinear biasing systems for dielectric elastomer actuators, Actuators 10 (9) (2021) 209, <https://doi.org/10.3390/act10090209>.
- [33] K.V. Poletkin, Z. Lu, U. Wallrabe, V. Badilita, A new hybrid micromachined contactless suspension with linear and angular positioning and adjustable dynamics, J. Microelectromech. Syst. 24 (2015) 1248–1250, <https://doi.org/10.1109/JMEMS.2015.2469211>.
- [34] K.V. Poletkin, A novel hybrid Contactless Suspension with adjustable spring constant, in: Proceedings of the International Conference on Solid-State Sensors, Actuators and Microsystems, TRANSDUCERS, 2017, pp. 934–937, <https://doi.org/10.1109/TRANSDUCERS.2017.7994203>.
- [35] K.V. Poletkin, J.G. Korvink, Modeling a pull-in instability in micro-machined hybrid contactless suspension, Actuators 7 (2018) 11, <https://doi.org/10.3390/act7010011>.
- [36] P.M. Weber, A. Schütz, T. Bechtold, U. Wallrabe, in: Cantilever free magnetic actuation for multistable vertical displacement, Proceedings of the MikroSystemeTechnik Kongress, VDE Verlag GmbH, Dresden, 2023, ISBN 978-3-8007-6203-3.
- [37] M. Olbrich, A. Schütz, T. Bechtold, C. Ament, Design and optimal control of a multistable, cooperative microactuator, Actuators 10 (8) (2021) 183, <https://doi.org/10.3390/act10080183>.
- [38] P.M. Weber, Y.T. Ruede, U. Wallrabe, Multistable magnetic lift actuation under variable loads, ACTUATOR 2024. International Conference and Exhibition on New Actuator Systems and Applications, Wiesbaden, Germany, 2024, pp. 120–123, 978-3-8007-6391-7.
- [39] H. Shahsavari, X. Chen, G.K. Tshikwanda, F. Wendler, M. Kohl, Finite-element analysis of an antagonistic bistable shape memory alloy beam actuator, Adv. Eng. Mater. 26 (2024) 202400969, <https://doi.org/10.1002/adem.202400969>.
- [40] L. Seigner, G.K. Tshikwanda, F. Wendler, M. Kohl, Bi-directional origami-inspired SMA folding microactuator, Actuators 10 (8) (2021) 181, <https://doi.org/10.3390/act10080181>.
- [41] L. Seigner, O. Bezsmertna, S. Fähler, G.K. Tshikwanda, F. Wendler, M. Kohl, Origami-inspired shape memory folding microactuator, Multidiscip. Digit. Publ. Inst. Proc. 64 (1) (2020) 6, <https://doi.org/10.3390/leCAT2020-08480>.
- [42] M. Sielenkämper, J. Dittmann, S. Wulfinhoff, Numerical strategies for variational updates in large strain inelasticity with incompressibility constraint, Int. J. Numer. Methods Eng. 123 (1) (2021) 245–267, <https://doi.org/10.1002/nme.6855>.
- [43] S.M. Curtis, M. Sielenkämper, G. Arivanandhan, D. Dengiz, Z. Li, J. Jetter, L. Hanke, L. Bumke, E. Quandt, S. Wulfinhoff, M. Kohl, TiNiHf/SiO₂/Si shape memory film composites for bi-directional micro actuation, Int. J. Smart Nano Mater. 13 (2) (2022) 293–314, <https://doi.org/10.1080/19475411.2022.2071352>.
- [44] M.B. Shamim, M. Hörsting, S. Wulfinhoff, Variational reduced-order modeling of thermomechanical shape memory alloy based cooperative bistable microactuators, Actuators 12 (1) (2023) 36, <https://doi.org/10.3390/act12010036>.
- [45] P. Conrad, A. Berdnykov, M. Hoffmann, Design of a liquid dielectrophoresis-driven platform with cooperative actuation, in: Proceedings of the International Conference and Exhibition on New Actuator Systems and Applications, ACTUATOR, 2022, pp. 182–185. ISBN: 978-3-8007-5894-4.

- [46] M. Duduta, E. Hajiesmaili, H. Zhao, R.J. Wood, D.R. Clarke, Realizing the potential of dielectric elastomer artificial muscles, *Proc. Natl. Acad. Sci.* 116 (7) (2019) 2476–2481, <https://doi.org/10.1073/pnas.1815053116>.
- [47] X. Ji, X. Liu, V. Cacuciolo, Y. Civet, A.E. Haitami, S. Cantin, Y. Perriard, H. Shea, Untethered feel-through haptics using 18- μ m thick dielectric elastomer actuators, *Adv. Funct. Mater.* 31 (39) (2021) 2006639, <https://doi.org/10.1002/adfm.202006639>.
- [48] Z. Ren, S. Kim, X. Ji, W. Zhu, F. Niroui, J. Kong, Y. Chen, A high-lift micro-aerial-robot powered by low-voltage and long-endurance dielectric elastomer actuators, *Adv. Mater.* 34 (7) (2022) 2106757, <https://doi.org/10.1002/adma.202106757>.
- [49] F. Carpi, G. Frediani, S. Turco, D. De Rossi, Bioinspired tunable lens with muscle-like electroactive elastomers, *Adv. Funct. Mater.* 21 (2011) 4152–4158, <https://doi.org/10.1002/adfm.201101253>.
- [50] G. Frediani, J. Busfield, F. Carpi, Enabling portable multiple-line refreshable Braille displays with electroactive elastomers, *Med. Eng. Phys.* 60 (2018) 86–93, <https://doi.org/10.1016/j.medengphy.2018.07.012>.
- [51] S. Hau, G. Rizzello, M. Hodgins, A. York, S. Seelecke, Design and control of a high-speed positioning system based on dielectric elastomer membrane actuators, *IEEE/ASME Trans. Mechatron.* 22 (3) (2017) 1259–1267, <https://doi.org/10.1109/TMECH.2017.2681839>.
- [52] S. Croce, J. Neu, G. Moretti, J. Hubertus, G. Schultes, G. Rizzello, Finite element modeling and validation of a soft array of spatially coupled dielectric elastomer transducers, *Smart Mater. Struct.* 31 (8) (2022) 084001, <https://doi.org/10.1088/1361-665X/ac78ad>.
- [53] J. Neu, J. Hubertus, S. Croce, G. Schultes, S. Seelecke, G. Rizzello, Fully polymeric domes as high-stroke biasing system for soft dielectric elastomer actuators, *Front. Robot. AI* 8 (2021) 695918, <https://doi.org/10.3389/frobt.2021.695918>.
- [54] R. Peltine, R. Kornbluh, Q. Pei, J. Joseph, High-speed electrically actuated elastomers with strain greater than 100%, *Science* 287 (5454) (2000) 836–839, <https://doi.org/10.1126/science.287.5454.836>.
- [55] J. Neu, J. Hubertus, S. Croce, G. Schultes, S. Seelecke, G. Rizzello, Fully polymeric domes as high-stroke biasing system for soft dielectric elastomer actuators, *Front. Robot. AI* 10 (8) (2021) 695918, <https://doi.org/10.3389/frobt.2021.695918>.
- [56] Lochmatter P., Development of a shell-like electroactive polymer (EAP) actuator. Ph. D. Diss., ETH-Nr. 17221 (2007).
- [57] J.P.L. Bigué, J.S. Plante, Experimental study of dielectric elastomer actuator energy conversion efficiency, *IEEE/ASME Trans. Mechatron.* 18 (1) (2013) 169–177, <https://doi.org/10.1109/TMECH.2011.2164930>.
- [58] J. Qiu, J.H. Lang, A.H. Slocum, A curved-beam bistable mechanism, *J. Microelectromech. Syst.* 13 (2) (2004) 137–146, <https://doi.org/10.1109/JMEMS.2004.825308>.
- [59] K. Poletkin, On the static pull-in of tilting actuation in electromagnetically levitating hybrid micro-actuator: theory and experiment, *Actuators* 10 (2021) 256, <https://doi.org/10.3390/act10100256>.
- [60] K.V. Poletkin, A. Asadollahbaik, R. Kampmann, J.G. Korvink, Levitating micro-actuators: a review, *Actuators* 7 (2) (2018) 17, <https://doi.org/10.3390/act7020017>.
- [61] I. Morkevnaite-Vilkonciene, V. Bucinskas, J. Subaciute-Zemaitiene, E. Sutinyas, D. Virzonis, A. Dziedzicki, Development of electrostatic microactuators: 5-year progress in modeling, design, and applications, *Micromachines* 13 (8) (2022) 1256, <https://doi.org/10.3390/mi13081256>.
- [62] I. Sari, M. Kraft, A MEMS linear accelerator for levitated micro-objects, *Sens. Actuators A Phys.* 222 (2015) 15–23, <https://doi.org/10.1016/j.sna.2014.11.008>.
- [63] W. Liu, W.Y. Chen, W.P. Zhang, X.G. Huang, Z.R. Zhang, Variable-capacitance micromotor with levitated diamagnetic rotor, *Electron. Lett.* 44 (11) (2008) 681–683, <https://doi.org/10.1049/el:20080528>.
- [64] Q. Xiao, K. Michael, Z. Luo, J. Chen, J. Wang, Design of contactless electromagnetic levitation and electrostatic driven rotation control system for a micro mirror, in: *Proceedings of the 15th International Conference on Control, Automation, Robotics and Vision (ICARCV)*, IEEE, 2018, <https://doi.org/10.1109/ICARCV.2018.8581285>.
- [65] K.V. Poletkin, Static pull-in behavior of micro-machined hybrid levitation actuators: modeling, simulation and experimental study, *IEEE/ASME Trans. Mechatron.* 26 (2) (2021) 753–764, <https://doi.org/10.1109/TMECH.2020.2999516>.
- [66] C. Ruffert, R. Gehrking, B. Ponick, H.H. Gatzert, Magnetic levitation assisted guide for a linear micro-actuator, *IEEE Trans. Magn.* 42 (11) (2006) 3785–3787, <https://doi.org/10.1109/TMAG.2006.879160>.
- [67] K.V. Poletkin, Simulation of static pull-in instability of hybrid levitation micro-actuators, in: *Proceedings of the ACTUATOR Conference 2021, Online Conference, February 16–19, 2021*, pp. 450–453. ISBN: 978-3-8007-5454-0.
- [68] C. Shearwood, K.Y. Ho, C.B. Williams, H. Gong, Development of a levitated micromotor for application as a gyroscope, *Sens. Actuators A Phys.* 83 (1–3) (2000) 85–92, [https://doi.org/10.1016/S0924-4247\(00\)00292-2](https://doi.org/10.1016/S0924-4247(00)00292-2).
- [69] E.R. Mamleyev, C.H. Lee, J.G. Korvink, M. Kohl, K.V. Poletkin, Experimental study and simulation of pull-in behavior in hybrid levitation microactuator for square-shaped proof masses, *Actuators* 12 (2023) 48, <https://doi.org/10.3390/act12020048>.
- [70] P.P. Udalov, I.A. Popov, A.V. Lukin, L.V. Shtukin, K.V. Poletkin, Parametric stability of microscale contactless inductive suspension with an electrostatic control loop of stiffness, *J. Mach. Manuf. Reliab.* 53 (2024) 25–34, <https://doi.org/10.1134/S1052618824010138>.
- [71] A.V. Lukin, I.A. Popov, P.P. Udalov, L.V. Shtukin, K.V. Poletkin, Quasi-static stability of microscale contactless inductive suspension with electrostatic stiffness control loop, *J. Appl. Comput. Mech.* (2024) 1–9, <https://doi.org/10.22055/JACM.2024.46862.4610>, in press.
- [72] E.R. Mamleyev, A. Voigt, A. Moazenzadeh, J.G. Korvink, M. Kohl, K.V. Poletkin, A technological approach for miniaturization of 3D inductive levitation micro-suspensions, *IEEE Magn. Lett.* 13 (2022) 1–4, <https://doi.org/10.1109/LMAG.2022.3174522>.
- [73] K.V. Poletkin, Z. Lu, A. Moazenzadeh, S. Guru Mariappan, J. Korvink, U. Wallrabe, V. Badilita, Polymer magnetic composite core boosts performance of 3D micromachined inductive contactless suspension, *IEEE Magn. Lett.* 7 (2016) 1–3, <https://doi.org/10.1109/LMAG.2016.2612181>.
- [74] Z. Lu, *Micromachined inductive suspensions with 3D wirebonded microcoils*, in: *Microactuators - Design and Technology*, 11, Shaker Verlag, Aachen, 2017. ISBN 9783844054507.
- [75] Y. Cao, M. Derakhshani, Y. Fang, G. Huang, C. Cao, Bistable structures for advanced functional systems, *Adv. Funct. Mater.* 31 (45) (2021) 1–23, <https://doi.org/10.1002/adfm.202106231>.
- [76] X. Wang, C. Zhi, Y. Li, M. Qu, Z. Xiong, Design and analysis of micro inertial switch with magnetic latch and adjustable threshold, *Microsyst. Technol.* 30 (2024) 1039–1048, <https://doi.org/10.1007/s00542-024-05652-9>.
- [77] J. Xu, Y. Leng, X. Su, X. Chen, F. Sun, Nonlinear dynamics and performance enhancement strategies for the magnetic levitating bistable electromagnetic energy harvester, *J. Vib. Eng. Technol.* 12 (2024) 3963–3976, <https://doi.org/10.1007/s42417-023-01099-w>.
- [78] S. Böhm, G.J. Burger, M.T. Korthorst, F. Roseboom, A micromachined silicon valve driven by a miniature bi-stable electro-magnetic actuator, *Sens. Actuators A Phys.* 80 (1) (2000) 77–83, [https://doi.org/10.1016/S0924-4247\(99\)00298-8](https://doi.org/10.1016/S0924-4247(99)00298-8).
- [79] J. Zhu, P. Han, C. Qi, G. Gong, H. Yang, T. Shinshi, D. Han, A single-coil-driven tristable electromagnetic mini valve with multiple working states, *Sens. Actuators A Phys.* 377 (2024) 1–13, <https://doi.org/10.1016/j.sna.2024.115699>.
- [80] Z. Zhang, X. Li, X. Yu, H. Chai, Y. Li, H. Wu, S. Jiang, Magnetic actuation bionic robotic gripper with bistable morphing structure, *Compos. Struct.* 229 (2019) 2–7, <https://doi.org/10.1016/j.compstruct.2019.111422>.
- [81] J. Zhao, R. Gao, G. Chen, S. Liu, Q. Cao, T. Qiu, Nonlinear coupling mechanical model for large stroke magnetic-based multistable mechanisms, *Mech. Mach. Theory* 83 (2015) 56–58, <https://doi.org/10.1016/j.mechmachtheory.2014.09.004>.
- [82] P.M. Weber, U. Wallrabe, M.C. Wapler, Self-sensing of a magnetically actuated prism, *Sensors* 23 (12) (2023) 5493, <https://doi.org/10.3390/s23125493>.
- [83] D. Vogtmann, R. St Pierre, S. Bergbreiter, Magnetic actuation of thick film multi-material compliant mechanisms, *J. Micromech. Microeng.* 27 (12) (2017) 125021, <https://doi.org/10.1088/1361-6439/aa946b>.
- [84] R. St Pierre, S. Bergbreiter, Gait exploration of sub-2 g robots using magnetic actuation, *IEEE Robot. Autom. Lett.* 2 (1) (2017) 34–40, <https://doi.org/10.1109/LRA.2016.2523603>.
- [85] M. Olbrich, P. Weber, U. Wallrabe, C. Ament, Optimized feedforward control of a multistable magnetic actuator, international conference and exhibition on new actuator systems and applications, *Actuator* (2024) 128–131. ISBN: 978-3-8007-6391-7.
- [86] A. Schütz, M. Olbrich, S. Hu, C. Ament, T. Bechtold, Parametric system-level models for position-control of novel electromagnetic free flight microactuator, *Microelectron. Reliab.* 119 (2021) 114062, <https://doi.org/10.1016/j.microrel.2021.114062>.
- [87] A. Schütz, T. Bechtold, Matrix interpolation-based parametric model order reduction of electromagnetic systems with translational movement, in: *Proceedings of the 24th International Conference on Thermal, Mechanical and Multi-Physics Simulation and Experiments in Microelectronics and Microsystems (EuroSimE)*, 2023, pp. 1–6, <https://doi.org/10.1109/EuroSimE56861.2023.10100820>.
- [88] A. Schütz, T. Bechtold, Model order reduction of an electromagnetic actuator with moving components via piecewise quadratic coupling, in: *Proceedings of the 25th International Conference on Thermal, Mechanical and Multi-Physics Simulation and Experiments in Microelectronics and Microsystems (EuroSimE)*, 2024, pp. 1–7, <https://doi.org/10.1109/EuroSimE60745.2024.10491476>.
- [89] M. Gao, Y. Wang, P. Wang, On formation, annihilation, and evolution of potential wells, and nonlinear phenomena of multi-magnet energy sink system, *Chaos* 34 (5) (2024) 1–27, <https://doi.org/10.1063/5.0198626>.
- [90] J.Y. Qian, H. Cong-Wei, L. Xiao-Juan, J. Zhi-Jiang, Actuation mechanism of microvalves: a review, *Micromachines* 11 (2) (2020) 172, <https://doi.org/10.3390/mi11020172>.
- [91] R.M. Bena, X.T. Nguyen, A.A. Calderón, A. Rigo, N.O. Pérez-Arancibia, SMARTI: a 60-mg steerable robot driven by high-frequency shape-memory alloy actuation, *IEEE Robot. Autom. Lett.* 6 (4) (2021) 8173–8180, <https://doi.org/10.1109/LRA.2021.3070246>.
- [92] Y. Chi, Y. Li, Y. Zhao, Y. Hong, Y. Tang, J. Yin, Bistable and multistable actuators for soft robots: structures, materials, and functionalities, *Adv. Mater.* 34 (19) (2022) 2110384, <https://doi.org/10.1002/adma.202110384>.
- [93] G.B. Stachowiak, P.G. McCormick, Shape memory behaviour associated with the R and martensitic transformations in a NiTi alloy, *Acta Metall.* 36 (2) (1988) 291–297, [https://doi.org/10.1016/0001-6160\(88\)90006-5](https://doi.org/10.1016/0001-6160(88)90006-5).
- [94] M. Babaei, S. Kim, C. Velez, D.K. Patel, S. Bergbreiter, Increasing the energy efficiency of NiTi Unimorph actuators with a 3D-printed passive layer, *J. MEMS* 29 (5) (2020) 797–803, <https://doi.org/10.1109/JMEMS.2020.3016176>.
- [95] P. Velvaluri, A. Soor, P. Plucinsky, R. Lima de Miranda, R.D. James, E. Quandt, Origami-inspired thin-film shape memory alloy devices, *Sci. Rep.* 11 (1) (2021) 90217, <https://doi.org/10.1038/s41598-021-90217-3>.

- [96] A. Firouzeh, J. Paik, Robogami: a fully integrated low-profile robotic origami, *J. Mech. Robot.* 7 (2) (2015) 021009, <https://doi.org/10.1115/1.4029491>.
- [97] K. Zheng, E. Gao, B. Tian, J. Liang, Q. Liu, E. Xue, Q. Shao, W. Wu, Modularized paper actuator based on shape memory alloy, printed heater, and origami, *Adv. Intell. Syst.* 4 (2022), <https://doi.org/10.1002/aisy.202200194>.
- [98] S.M. Felton, M.T. Tolley, B.H. Shin, C.D. Onal, E.D. Demaine, D. Rus, R.J. Wood, Self-folding with shape memory composites, *Soft Matter* 9 (32) (2013) 7688–7696, <https://doi.org/10.1039/C3SM51003D>.
- [99] M.T. Tolley, S.M. Felton, S. Miyashita, D. Aukes, D. Rus, R.J. Wood, Self-folding origami: shape memory composites activated by uniform heating, *Smart Mater. Struct.* 23 (2014), <https://doi.org/10.1088/0964-1726/23/9/094006>.
- [100] Y. Kim, T. Jang, H. Gurung, N.A. Mansour, B. Ryu, B. Shin, Bidirectional rotating actuators using shape memory alloy wires, *Sens. Actuators A Phys.* 295 (2019) 512–522, <https://doi.org/10.1016/j.sna.2019.05.047>.
- [101] W. Wang, H. Rodrigue, S.H. Ahn, Deployable soft composite structures, *Sci. Rep.* 6 (2016) 20869, <https://doi.org/10.1038/srep20869>.
- [102] J.K. Paik, R.J. Wood, A bidirectional shape memory alloy folding actuator, *Smart Mater. Struct.* 21 (2012) 065013 (8pp).
- [103] G. Arivanandhan, Z. Li, S.M. Curtis, P. Velvaluri, E. Quandt, M. Kohl, Temperature homogenization of co-integrated shape memory–silicon bimorph actuators, *Multidiscip. Digit. Publ. Inst. Proc.* 64 (1) (2020) 8, <https://doi.org/10.3390/iecat2020-08501>.
- [104] M. Kohl, Shape Memory Microactuators, Springer Science & Business Media, 2004, <https://doi.org/10.1007/978-3-662-09875-2>.
- [105] L. Seigner, V. Gottwald, L. Bumke, E. Quandt, M. Kohl, Enhanced bi-directional SMA actuation of origami-inspired microstructures, in: *Proceedings of the MikroSystemTechnik Kongress 2023, Dresden, Deutschland, 2023*, pp. 820–824.
- [106] V. Gottwald, L. Seigner, M. Ohtsuka, M. Kohl, Origami-inspired bistable SMA microdevice, in: *Proceedings of the SMST 2024: Extended Abstracts from the International Conference on Shape Memory and Superelastic Technologies, Cascais, Portugal, ASM, 2024*, pp. 74–75, <https://doi.org/10.31399/asm.cp.smst2024p0074>, May 6–10.
- [107] G.K. Tshikwand, L. Seigner, F. Wendler, M. Kohl, Coupled finite element simulation of shape memory bending microactuator, *Shape Mem. Superelast.* 8 (2022) 373–393, <https://doi.org/10.1007/s40830-022-00396-9>.
- [108] M. Kostov, T. Todorov, R. Mitrev, K. Kamberov, R. Nikolov, A study of a bistable reciprocating piston pump driven by shape memory alloys and recuperative springs, *Actuators* 12 (2) (2023) 90, <https://doi.org/10.3390/act12020090>.
- [109] Y. Wan, K. Cuff, M.J. Serpe, A wirelessly controlled shape-memory alloy-based bistable metal swimming device, *Adv. Intell. Syst.* 4 (5) (2022) 101365, <https://doi.org/10.1002/aisy.202100251>.
- [110] J.S. Koh, E. Yang, G.P. Jung, S.P. Jung, J.H. Son, S.I. Lee, P.G. Jablonski, R. J. Wood, H.Y. Kim, K.J. Cho, Jumping on water: surface tension-dominated jumping of water striders and robotic insects, *Science* 349 (6247) (2015) 517–521, <https://doi.org/10.1126/science.aab1637>.
- [111] F. Lambrecht, C. Lay, I.R. Aseguinolaza, V. Chernenko, M. Kohl, NiMnGa/Si shape memory bimorph nanoactuation, *Shape Mem. Superelast.* 2 (2016) 347–359, <https://doi.org/10.1007/s40830-016-0080-1>.
- [112] M. Kohl, M. Schmitt, A. Backen, L. Schultz, B. Krevet, S. Fähler, Ni-Mn-Ga shape memory nano actuation, *Appl. Phys. Lett.* 104 (4) (2014) 043111, <https://doi.org/10.1063/1.4863667>.
- [113] S. Rastjoo, R. Fechner, L. Bumke, M. Kötz, E. Quandt, M. Kohl, Development and co-integration of a SMA/Si bimorph nanoactuator for Si photonic circuits, *Microelectron. Eng.* 225 (2020) 111257, <https://doi.org/10.1016/j.mee.2020.111257>.
- [114] F. Lambrecht, I. Aseguinolaza, V. Chernenko, M. Kohl, Integrated SMA-based NEMS actuator for optical switching, in: *Proceedings of the MEMS'16, Shanghai, China, 2016*, <https://doi.org/10.1109/MEMSYS.2016.7421562>.
- [115] S. Mühlbrandt, A. Melikyan, T. Harter, K. Köhnle, A. Muslija, P. Vincze, S. Wolf, P. Jakobs, Y. Fedoryshyn, W. Freude, J. Leuthold, C. Koos, M. Kohl, Silicon-plasmonic internal-photoemission detector for 40 Gbit/s data reception, *Optica* 3 (7) (2016) 741–747, <https://doi.org/10.1364/OPTICA.3.000741>.
- [116] B. Winzek, T. Sterzl, E. Quandt, Bistable thin film composites with TiHfNi-shape memory alloys, in: *Proceedings of the Transducers'01, Eurosensors, 2001*, pp. 706–709, https://doi.org/10.1007/978-3-642-59497-7_168.
- [117] B. Winzek, S. Schmitz, H. Rumpf, T. Sterzl, R. Hassdorf, S. Thienhaus, J. Feydt, M. Moske, E. Quandt, Recent developments in shape memory thin film technology, *Mater. Sci. Eng. A* 378 (1–2) (2004) 40–46, <https://doi.org/10.1016/j.msea.2003.09.105>.
- [118] G. Arivanandhan, Z. Li, S.M. Curtis, L. Hanke, E. Quandt, M. Kohl, Power optimization of TiNiHf/Si shape memory microactuators, *Actuators* 12 (2) (2023) 82, <https://doi.org/10.3390/act12020082>.
- [119] F. Lambrecht, N. Sagardiluz, M. Gueltig, I.R. Aseguinolaza, V. Chernenko, M. Kohl, Martensitic transformation in NiMnGa/Si bimorph nanoactuators with ultra-low hysteresis, *Appl. Phys. Lett.* 110 (21) (2017) 213104, <https://doi.org/10.1063/1.4984058>.
- [120] H. Geng, S.K. Cho, Dielectrowetting for digital microfluidics: principle and application. A critical review, *Rev. Adhes. Adhes.* 5 (3) (2017) 268–302, <https://doi.org/10.1002/9781119526445.ch7>.
- [121] S. Günther, S. Si, H. D'heer, D. van Thuurhout, M. Hoffmann, FDTS as dewetting coating for an electrowetting controlled silicon photonic switch, *IEEE Photonics Technol. Lett.* 30 (23) (2018) 2005–2008, <https://doi.org/10.1109/LPT.2018.2874351>.
- [122] L. Schmitt, P. Conrad, A. Kopp, C. Ament, M. Hoffmann, Non-inchworm electrostatic cooperative micro-stepper-actuator systems with long stroke, *Actuators* 12 (4) (2023) 150, <https://doi.org/10.3390/act12040150>.
- [123] M.L. Chan, B. Yoxall, H. Park, Z. Kang, I. Izyumin, J. Chou, M.M. Megens, M. C. Wu, B.E. Boser, D.A. Horsley, Design and characterization of MEMS micromotor supported on low friction liquid bearing, *Sens. Actuators A* 177 (2012) 1–9, <https://doi.org/10.1016/j.sna.2011.08.003>.
- [124] H. Kang, J. Kim, EWOD (Electrowetting-On-Dielectric) actuated optical micromirror, in: *Proceedings of the MEMS Conference, 2006*, pp. 742–745, <https://doi.org/10.1109/MEMSYS.2006.1627906>.
- [125] A.M. Kopp, P. Conrad, M. Hoffmann, C. Ament, System level modeling and closed loop control for a droplet-based micro-actuator, in: *Proceedings of the SICE International Symposium on Control Systems (SICE ISCS), IEEE, 2023*, pp. 33–40, <https://doi.org/10.23919/SICEISCS57194.2023.10079205>.
- [126] J. Berthier, K.A. Brakke, *The Physics of Microdroplets*, Wiley, 2012, <https://doi.org/10.1002/9781118401323>.
- [127] B. Ahn, K. Lee, R. Louge, K.W. Oh, Concurrent droplet charging and sorting by electrostatic actuation, *Biomicrofluidics* 3 (4) (2009) 44102, <https://doi.org/10.1063/1.3250303>. PMID: 20216964; PMCID: PMC2835282.
- [128] S. Lee, S. Lee, H. Hwang, J. Hong, S. Lee, J. Lee, Y. Chae, T. Lee, Ultrafast single-droplet bouncing actuator with electrostatic force on superhydrophobic electrodes, *RSC Adv.* 6 (71) (2016) 66729–66737, <https://doi.org/10.1039/c6ra12092j>.
- [129] E. Samiei, M. Tabrizian, M. Hoorfar, A review of digital microfluidics as portable platforms for lab-on-a-chip applications, *Lab Chip* 16 (2016) 2376–2396, <https://doi.org/10.1039/C6LC00387G>.
- [130] B. Shapiro, H. Moon, R.L. Garrell, C.J. Kim, Equilibrium behavior of sessile drops under surface tension, applied external fields, and material variations, *J. Appl. Phys.* 93 (9) (2003) 5794–5811, <https://doi.org/10.1063/1.1563828>.
- [131] IEEE-DEIS-EHD Technical Committee, Recommended international standard for dimensionless parameters used in electrohydrodynamics, *IEEE Trans. Dielectr. Electr. Insul.* 10 (1) (2003) 3–6, <https://doi.org/10.1109/TDEI.2003.1176545>.
- [132] S. Günther, S. Gropp, M. Hoffmann, H. D'heer, D. van Thuurhout, A. Neft, F. Bartels, K. Gradkowski, L. Carroll, P. O'Brien, C. Lerma-arce, J. Watté, Electrowetting controlled non-volatile integrated optical switch, in: *Proceedings of the European Conference on Optical Communication (ECOC), 2018*, p. 3, <https://doi.org/10.1109/ECOC.2018.8535585>.
- [133] X. Wu, D. Tang, Q. He, L. Liu, Z. Jia, Y. Tan, Research progress of electrode shapes in EWOD-based digital microfluidics, *RSC Adv.* 13 (25) (2023) 16815–16827, <https://doi.org/10.1039/d3ra01817b>.
- [134] K. Poletkin, Z. Lu, U. Wallrabe, J. Korvink, V. Badilita, Stable dynamics of micro-machined inductive contactless suspensions, *Int. J. Mech. Sci.* 131–132 (2017) 753–766, <https://doi.org/10.1016/j.ijmecsci.2017.08.016>.
- [135] E.R. Mamleyev, M. Kohl, J.G. Korvink, K.V. Poletkin, Fabrication process of conventional and unconventional 3D microcoils based on 2D array of SU-8 microposts structure, in: *Proceedings of the 22nd International Conference on Solid-State Sensors, Actuators and Microsystems, Transducers, 2023*, pp. 883–886. ISBN: 978-4-88686-435-2.